ELSEVIER

Contents lists available at ScienceDirect

Quaternary Science Reviews

journal homepage: www.elsevier.com/locate/quascirev





Using luminescence dating to constrain lake sediment records: A new age model for the 1.38 Ma lake Malawi drill core, Eastern Africa

Laura C. Streib a, , Simon J. Armitage b, c, Christopher A. Scholz a

- ^a Department of Barth and Environmental Sciences, Syracuse University, Syracuse, NY, 13244, USA
- b Department of Geography, Royal Holloway, University of London, Egham, Surrey, TW20 OEX, UK
- ^c SFF Centre for Early Sapiens Behaviour (SapienCE), University of Bergen, Post Box 7805, 5020, Bergen, Norway

ARTICLE INFO

Handling editor: Giovanni Zanchetta

ABSTRACT

The 2005 Lake Malawi deep scientific drill core is the longest and most continuous high-resolution record from the continental tropics, extending to ~ 1.38 Ma. While extensive sets of paleoclimate proxy data have been generated from this core, a gap in directly dated sediment, between ~ 74 ka and ~ 590 ka (28–167 m below lake floor), has limited the understanding of climatic drivers in this system. Previous age models fill the gap in direct dates by tuning to the global 5^{18} O stack and interpreting paleomagnetic excursions, but these methods and the resulting models remain disputed. We fill this gap in chronology using luminescence dating, with 31 samples collected at ~ 4 m resolution in this section of the core. Luminescence dating can sometimes be limited by relatively large uncertainties (typically ~ 796) and difficulty estimating the water content history of samples. We overcome these limitations by employing a high sampling density and using the sediment record to understand changes in water content during the burial period. This yields a vastly improved and robust age model that indicates changes in sedimentation rates not discernible in prior age models.

1. Introduction

Bastern Africa was a key site of hominin evolution and development, with the regional environment likely playing a role in evolving morphology, life history, social behavior, and migration (Maslin et al., 2015). The same region today is home to ~400 million people, with the population expected to more than double by 2050 (United Nations, 2019). This rapidly growing population is especially vulnerable to climate change, with dependence on rain-fed agriculture, low adaptive capacity, privatization of resources, conflict, and disease putting inhabitants at particular risk (Fields, 2005; Thomas and Nigam, 2018). To understand the context and causes of early human development and protect human populations today, we need to understand what drives long-term changes in climate in this key region.

Several different hydroclimatic driving mechanisms have been proposed over multimillennial scales. Most often discussed are regional insolation (Trauth et al., 2003; Ivory et al., 2016), high latitude forcing (Tierney et al., 2008; Castañeda et al., 2016), or a combination of the two (Trauth et al., 2007; Lyons et al., 2015; Caley et al., 2018; Lamb et al., 2018; Owen et al., 2018; Foerster et al., 2022; Lupien et al., 2022). On decadal to sub-centennial time scales, changes to the bipolar seesaw,

El Niño-Southern Oscillation, tropical rain belt migration, Indian Ocean Dipole, Congo Air Boundary migration, and sunspot cycles have all been invoked to explain and describe climatic variability (Lean et al., 1995; Brown et al., 2007; Russell and Johnson, 2007; Tierney et al., 2011, 2013; Wolff et al., 2011).

Determining climatic drivers in the region has been hindered by a lack of long-duration high-resolution records (Trauth et al., 2005; Scholz et al., 2007; Lupien et al., 2021). The ~1.38 Ma sediment core collected from Lake Malawi in 2005 exhibits prominent climatic signals, which have been widely published (Fig. 1) (Scholz et al., 2006; Stone et al., 2011; Lyons et al., 2015; Johnson et al., 2016; Ivory et al., 2016, 2018). As the longest continuous record collected from the continental tropics to date, it should help resolve the debate on climatic drivers in the region. The use of this record, however, has been limited by a lack of directly dated sediments between ~74 ka and ~590 ka (28–167 m core depth) (Fig. 2). Here we use luminescence dating of feldspar grains to address this outstanding problem.

Luminescence dating has been successfully applied to a wide range of archaeological and geological sedimentary deposits (Jacobs and Roberts, 2007; Wintle, 2008). Early work was mostly applied to aeolian material where sufficient sunlight exposure could be assumed, typically

E-mail addresses: lcstreib@syr.edu (L.C. Streib), simon.armitage@rhul.ac.uk (S.J. Armitage), cascholz@syr.edu (C.A. Scholz).

^{*} Corresponding author.

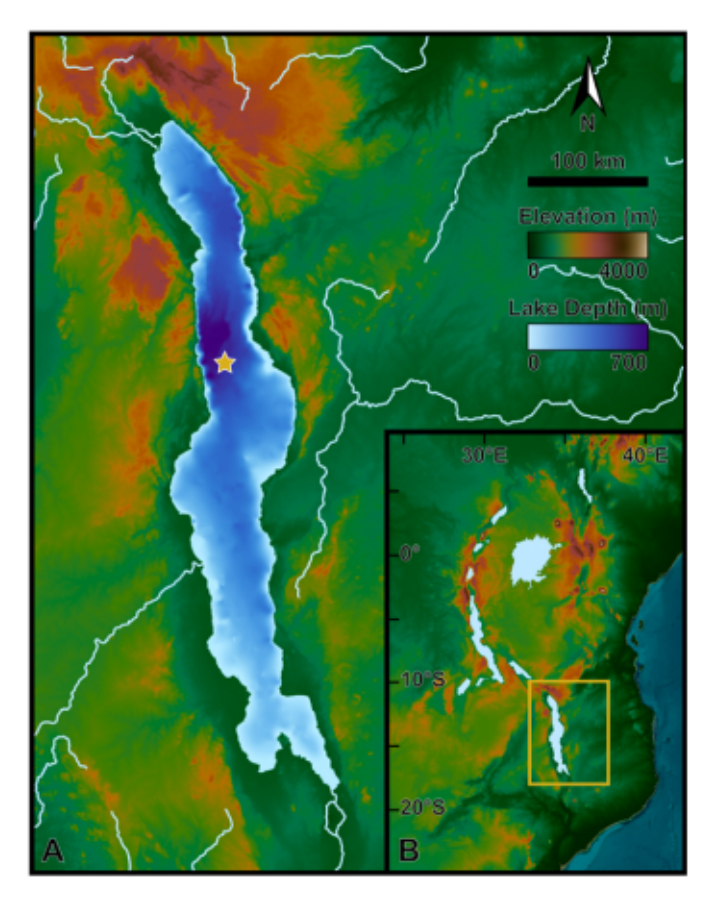


Fig. 1. A: Surrounding elevation and lake bathymetry of Lake Malawi, with the coring site identified as a yellow star. B: Regional overview with Lake Malawi highlighted in yellow. Bathymetry is from Scholz and Lyons (2022), rivers are from World Agroforestry Centre (2014), and topography is from Farr and Kobrick (2000).

measuring quartz from samples < 100 ka (Duller, 2008). More recently, the applicable age range of luminescence dating has been expanded via the use of new feldspar measurement protocols (Thomsen et al., 2008; Li et al., 2014) and the technique has been successfully applied to a broader range of environments, including lacustrine records (Buylaert et al., 2013; Roberts et al., 2018, 2021).

Until the last decade projects using luminescence dating on lake cores were largely exploratory and designed to test feasibility. Use of the technique in this setting has been limited by fears about partial bleaching of sediments, light exposure during sampling, and obtaining accurate water content histories (Roberts et al., 2018). Through time, these concerns have proven to be largely unfounded. Early work showed that luminescence dating was feasible in lake cores, though there were doubts that it could be applied to all sediments with insufficient sunlight exposure (partial bleaching) prior to deposition being the principal concern (Berger and Easterbrook, 1993; Berger and Anderson, 1994; Berger and Doran, 2001). Later work showed that partial bleaching, while still a concern, is not as prohibitive a factor as initially thought and is often only a serious impediment for samples younger than ~1 ka (Jain et al., 2004; Duller, 2008). Others have shown that while care must be taken to measure or calculate water content, it is no more of a challenge in lacustrine settings than in other environments where luminescence dating is more widely applied (Lukas et al., 2012; Roberts et al., 2018). Likewise, light exposure during sampling has also proven not to be a limiting factor, with Armitage and Pinder (2017) demonstrating that only the outer ~1 mm of sediment in a split core is exposed to sufficient light to produce age underestimates. In recent years luminescence dating has produced robust lacustrine age models with ever-increasing

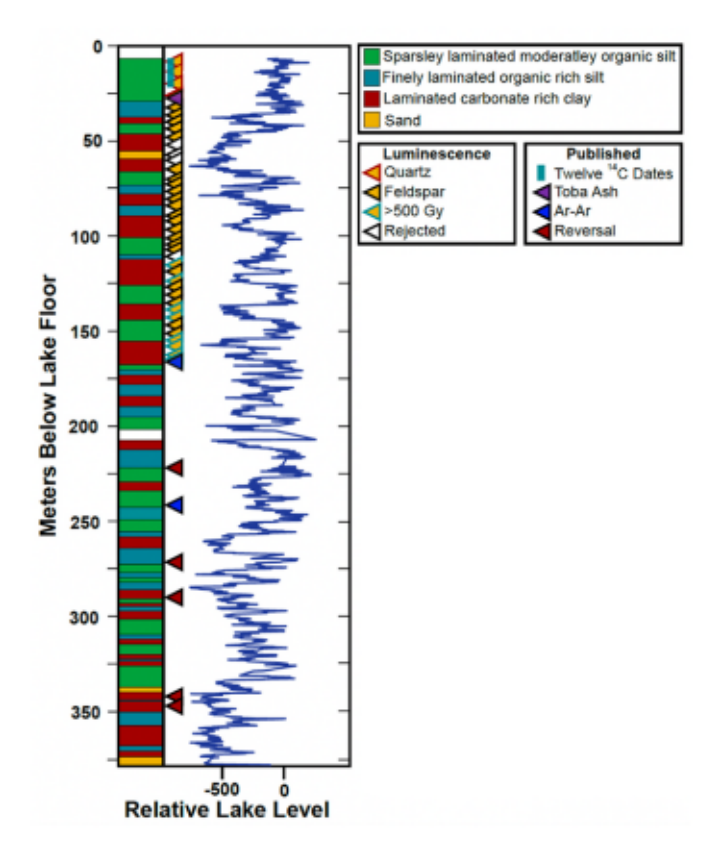


Fig. 2. A composite stratigraphic column of cores GLAD7-Mal05-1B and GLAD7-Mal05-1C with all dates included in the age model marked. Beside the column is the Lyons et al. (2015) calibrated lake level curve that utilized principal component analysis (PCA) on Ca, total organic carbon (TOC), δ^{13} C, saturated bulk density, and lightness of color datasets.

maximum age ranges (Buylaert et al., 2013; Roberts et al., 2018, 2021).

Chronology is a well-known challenge for sediment records, with date density and age modeling techniques often not sufficient for making robust interpretations about climatic drivers or relationships between records from different localities (Blaauw et al., 2018; Zimmerman and Wahl, 2020). While luminescence dating has limitations, namely a relatively high age uncertainty of 5-10%, it is well suited to help solve this problem. The main gaps left by other forms of dating, including limited age ranges (e.g., 14C, paleomagnetic dating), limited material (14C, Ar-Ar, tephra fingerprinting, U-Th), and reliance on assumptions, particularly that of uninterrupted deposition (paleomagnetic dating, tuning to presumed drivers), can be filled by luminescence dating. Luminescence dating can be performed on ubiquitous quartz and feldspar grains, is independent of other methods, and can be effective on samples aged less than 1 ka to greater than 600 ka (Thomsen et al., 2008; Buylaert et al., 2012; Arnold et al., 2015). With recent improvements in measurement techniques, luminescence dating is well suited to date the long sediment record from Lake Malawi as well as similar records.

1.1. Drill core from the lake Malawi scientific drilling project

The 2005 Lake Malawi Scientific Drilling Project acquired a composite core that extends to 380 m below lake floor (mblf), with a basal age of ~1.38 Ma, which is extrapolated from the identification of the Cobb Mountain paleomagnetic reversal ~345 mblf (Scholz et al., 2006; Lyons et al., 2015). While extensive sets of paleoclimate proxy data have been generated for this core, GLAD7-Mal05-1, there is a gap in directly dated sediments, roughly between 74 ka and 590 ka (28–167 mblf) (Fig. 2). An initial age model circumvented this gap in age determinations by linearly interpolating between the Youngest Toba Tuff

(28.09 mblf, 73.7 0.3 ka) and paleomagnetic excursion 15a (167.5 mblf, ~575 ka) and a nearby Ar Ar age of volcanic tephra (166.6 mblf, 20 ka) (Lane et al., 2013; Lyons et al., 2015; Mark et al., 2017). Alternative models fill the gap using paleomagnetic excursions and paleointensity data (Ivory et al., 2016) or tuning Tex₈₆-based temperature to the global ¹⁸O stack (Johnson et al., 2016). The excursion and intensity-based model utilizes a noisy paleomagnetic record and requires significant changes in sedimentation rate that are not supported by changes in sediment composition or the adjacent seismic stratigraphic framework (e.g. Lyons et al., 2011). In noisy paleomagnetic records, errors can occur where an excursion is absent or misidentified, which then produces an age offset between the modelled and true age for all deeper levels in the core. The TEX_{86} ¹⁸O tuned age model assumes that regional temperatures follow global trends, which may be the case, but then invokes a circular argument when using the record to determine climatic drivers. Using the Tex_{86} ^{18}O correlation incorporates additional uncertainty into the model since lake surface temperatures must be corrected for the dry adiabatic lapse rate, because lake level fluctuates hundreds of meters over the course of the record. Moreover, all the published age models are based on lines of best fit through dates and do not use Bayesian methods to quantify and minimize uncertainties in the models. Presenting known uncertainty is necessary to quantitatively assess potential drivers of climatic change (Blaauw et al., 2018; Zimmerman and Wahl, 2020). We solve this outstanding set of problems using luminescence dating and a Bayesian age model to fill the gap in chronology.

2. Regional setting

Lake Malawi is one of the largest lakes in the world, covering \sim 30,000 km² with a present-day maximum depth of 700 m, and sits at the southern end of the East African Rift System (Fig. 1). The lake partially fills the Malawi Rift, a series of linked asymmetric half-graben basins that initially formed in the late Cenozoic (Scholz et al., 2020). Normal faulting and extension control the morphology of the basin, and sediment delivery and accumulation in some parts of the lake (Scholz et al., 2020). In the northern and central basins, major border faults produce steep slopes both onshore and within the lake, whereas the far southern and southwestern shorelines have more gradual bathymetric gradients (Eccles, 1974; Lyons et al., 2011; Scholz and Lyons, 2022). Today, the quantity and seasonality of precipitation is driven by the path of the tropical rain belt. Lake Malawi sits at the southern end of the rain belt track, at 9 14 S, such that it experiences a single rainy season in austral summer and one dry and windy season in austral winter (Eccles, 1974; Owen and Crossley, 1992).

Because of the vast size of the lake, precipitation varies greatly over its extent. Annual rainfall in southern parts of the lake is 65 cm/yr, while the central basin and northern extremity receive 200 and 250 cm/yr, respectively (Eccles, 1974). Direct evaporation accounts for 80% of water loss, and the remainder flows out from the Shire River through the southeastern arm of the lake (Owen and Crossley, 1992). Though near the equator, the region experiences some temperature changes throughout the year, varying several degrees Celsius between winter and summer months (Eccles, 1974). Localities near the northern and southern ends of the lake experience a wider range of annual temperatures than localities near the center of the basin, where the lake moderates climate (Eccles, 1974). Today the lake is permanently stratified, with the boundary between the oxic and anoxic layers at ~220 m (Vollmer et al., 2005). Annually, the windy dry season cools surface waters and increases physical mixing in the upper waters (Owen and Crossley, 1992; Pilskaln, 2004; Vollmer et al., 2005). These high winds blow from the south along the axis of the lake at speeds of 40 km/h for intervals of several days, resulting in surface waves of 3 4 m (Eccles, 1974).

3. Materials and methods

3.1. Sample collection

Subsamples from the archived drill core were collected under white light at the University of Minnesota Continental Scientific Drilling Facility where the cores have been stored since collection (University of Minnesota National Lacustrine Core Repository, 1996). An initial set of six samples was collected as part of a blind trial (Lab ID s containing a single letter), with four of these overlapping with the ¹⁴C dated portion of the core and two within the interval of interest. The bulk of the luminescence samples (Lab IDs prefixed $\,$ Mal- $\,$) were collected at a ~ 4 m resolution from 32 to 165 mblf, totaling 33 samples (Tables 2 and 3). Sample locations were selected to avoid changes in sedimentation rate, sections of apparent disturbance during coring, and cracks in the dried core face. Sample collection methods followed that of Armitage and Pinder (2017). Samples were collected by inserting 2.54 cm diameter copper tubes that had been stoppered with foam, into the split core face. The tubes were inserted until they made contact with the core liner, ~ 3 cm deep, yielding sample volumes of \sim 15 ml. The full sample tubes were sealed with duct tape and wrapped in aluminum foil to prevent light penetration.

Sample preparation and measurement were conducted at the Royal Holloway Luminescence Laboratory. Samples were extruded under subdued red light and the outer \sim 0.5 cm on both ends of each sample tube were removed. This removed both the light-exposed portion at the cut core face and any material that may have suffered from barrel smear during coring (Armitage and Pinder, 2017).

3.2. Dose rate determination

The light exposed portions removed from the cut core face end of each sample were reserved and used for U, Th, and K measurements via ICP-MS (Th and U) and ICP-AES (K) at SGS Canada Inc (Lab IDs prefixed Mal-) or alpha and beta counting at the Royal Holloway Luminescence Laboratory (Lab ID s containing a single letter). Because samples were collected at core depths intended to avoid major stratigraphic changes, the material surrounding each sample was assumed to be homogenous with respect to gamma emitters, allowing gamma dose rates to be calculated from sample radioisotope concentrations. Given the modern

Table 1
The measurement protocols for quartz optically stimulated luminescence (OSL) (a) and polymineral post-infrared, infrared-stimulated luminescence (pIRIR) (b) samples. Test doses for steps a4 and b5 varied between 46.1 and 49.9 Gy.

	•	•
Step	a) Quartz OSL	b) Polymineral pIRIR
1	Give regenerative dose, D _i ^a	Give regenerative dose, D _i ^a
2	Preheat 1 (220 C for 10 s)	Preheat 1 (255 C for 60 s)
3	Blue diode stimulation (125 °C, 60 s), L_x^b	IR diode stimulation (60 C for 200 s)
4	Give test dose, D_t (~50 Gy)	IR diode stimulation (225 °C for 200 s), L_x^b
5	Preheat 2 (160 C for 5 s)	Give test dose, D _t (~50 Gy)
6	Blue diode stimulation (125 C, 60 s), T _x	Preheat 2 (255 C for 60 s)
7	Return to step 1	IR diode stimulation (60 C for 200 s)
8		IR diode stimulation (225 °C, 200 s), T_x^b
9		IR diode stimulation (290 C for 150 s)
10		Return to step 1

 $^{^{\}rm a}$ In the first cycle, where the natural luminescence intensity is observed, $D_{\rm i}$ 0 Gy.

 $[^]b$ For quartz, the luminescence signal (L_x or T_x) was that recorded during the first 0.32 s of stimulation, with a background signal from the last 10 s of stimulation subtracted; whereas for polymineral samples the signal was that recorded during the first 20 s minus a background signal from the last 20 s of stimulation.

 $\label{thm:controller} \textbf{Table 2} \\ \textbf{This table provides the data used to calculate the total dose rate for each sample, including the corrected water content and the concentrations of K, U, and Th. Sample water content and composite depth are provided for reference.} \\$

Lab ID	Composite depth (mblf)	Water con	itent (%)	Radioisotope concentrations			
		Sample ^a	Corrected ^b	K (%)	U (ppm)	Th (ppm)	
M ^c	8.31	210	211	1.7	1.2 0.2	9.0 1.0	
A ^c	13.55	205	206	0.2 1.6	1.8 0.2	7.1 1.0	
L ^c	19.78	213	215	0.1 1.5	1.6 0.3	9.3 1.2	
Sc	26.14	207	209	0.2 1.3	1.5 0.1	2.8 0.6	
MAL1	32.46	208	210	0.1 1.0	4.0 0.2	11.7 0.6	
MAL13	36.60	191	193	0.1 1.4	4.2 0.2	18.0 0.9	
MAL23	40.10	191	194	0.1 1.4	4.1 0.2	16.7 0.8	
MAL2	43.61	219	222	0.1 1.2	5.4 0.3	13.7	
MAL14	48.09	191	194	0.1 1.5	5.0	16.0	
MAL24 ^d	51.90	171	174	0.1 1.6	0.2 4.3	0.8	
MAL3 ^d	57.30	132	136	0.1 1.8	2.8	0.7	
MAL15 ^d	60.09	126	130	0.1 1.8	0.1 2.8	0.8 14.5	
MAL25	64.93	152	156	0.1 1.4	6.4	0.7	
MAL4	70.07	200	205	0.1 1.1	3.2	13.2	
MAL16	72.64	194	199	0.1 1.4	3.3	12.7	
E	74.43	171	177	0.1 1.2	0.2 4.6	0.6	
MAL26	80.43	205	210	0.2 1.6	0.5 4.2	2.1 14.6 0.7	
MAL5	83.86	176	182	0.1 1.4	0.2 4.2 0.2	14.8	
MAL27	89.15	166	172	0.1 1.4	5.8	0.7	
MAL6	91.99	171	177	0.1 1.5	0.3	0.7	
MAL17	96.50	172	178	0.1 1.7	0.2 4.0	0.8 15.4	
MAL28	101.05	208	216	0.1 1.3	0.2 3.6	0.8 12.9	
MAL7	104.37	195	203	0.1 1.2	0.2 4.4	0.6 15.0	
				0.1	0.2	0.8	

Table 2 (continued)

Lab ID	Composite depth (mblf)	Water con	itent (%)	Radioisotope concentrations			
		Sample ^a	Corrected ^b	K (%)	U (ppm)	Th (ppm)	
MAL29	107.09	192	201	1.3	4.1 0.2	13.7 0.7	
				0.1			
P ^d	110.75	171	180	1.8	2.2 0.4	13.1 1.6	
				0.2			
MAL18 ^e	115.23	165	172	1.7	4.1 0.2	14.2 0.7	
				0.1			
MAL8	118.54	185	193	1.5	4.5 0.2	14.4 0.7	
				0.1			
MAL31 ^e	123.49	160	168	1.6	4.0 0.2	14.2 0.7	
				0.1			
MAL19	126.75	172	181	1.3	3.8 0.2	13.6 0.7	
				0.1			
MAL9	130.71	193	203	1.0	3.7 0.2	12.4 0.6	
				0.1			
MAL32	135.13	182	192	1.3	5.5 0.3	13.9 0.7	
				0.1			
MAL20 ^d	138.70	167	175	1.7	4.1 0.2	15.0 0.8	
				0.1			
MAL10 ^e	142.74	175	184	1.4	3.4 0.2	14.8 0.7	
				0.1			
MAL33	146.72	191	201	1.2	3.7 0.2	11.7 0.6	
				0.1			
MAL21	151.11	186	197	1.2	4.0 0.2	13.0 0.7	
				0.1			
MAL11 ^e	154.78	157	166	1.8	3.5 0.2	14.6 0.7	
				0.1			
MAL34 ^e	157.87	187	196	1.7	4.5 0.2	14.5 0.7	
				0.1			
MAL22 ^e	162.49	158	167	1.4	4.4 0.2	14.1 0.7	
				0.1			
MAL12 ^e	164.90	170	179	1.6	3.6 0.2	14.0 0.7	
				0.1			

 $^{^{\}rm a}$ Sample refers to the water content calculated for the individual sample using steps 1 $\,$ 5 from Section 3.6.

depth of the coring site of 590 m lake depth, the cosmic dose rate was considered to be negligible and was not included in calculations (Prescott and Hutton, 1994). Based on the Lyons et al. (2015) lake level curve, the largest cosmic dose rate for any sample included in the age model was 0.01 0.001 Gy/ka on deposition and the mean for all samples was 0.001 0.0001 Gy/ka on deposition. After deposition, as each sample was buried by a growing sediment package, the cosmic dose rate declined further, thus the mean cosmic dose rate for the entire burial period of each sample is even lower than these values.

An alpha efficiency (a-value) of 0.04 0.02 was assumed for both quartz and feldspar. Conventionally, a-values of 0.04 0.02 and 0.086

b Corrected refers to the water content calculated using steps 1 6 in Section 3.6 and represents a temporal mean water content for the entire burial period.

^c Ages based on quartz measurements; all others are based on feldspar.

^d Dates representing reworked material that were removed from the age model.

 $^{^{\}rm e}\,$ Dates with equivalent doses $\,$ 500 Gy included in the age model as minimum ages.

Table 3

The dose rate for each type of radiation, total dose rate, equivalent dose, and calculated age of each sample. The reported errors represent 2 uncertainty. Most samples had six aliquots used for age determination. The exceptions, Mal1-Mal10, had nine aliquots. The number of aliquots was reduced from nine to six in later samples, because there was little variability between aliquots. No aliquots were removed because they failed screening tests. Equivalent dose is the arithmetic mean of the individual measurements of each aliquot. The youngest four samples M, A, L, and S are based on quartz measurements, all others are based on feldspar.

Lab ID	Composite depth (mblf)	Dose rates (Gy/ka) ^a					Total dose rate (Gy/ka)		Equivalent dose (Gy)		Age (ka)		
M ^b	8.31	0.09	0.03	0.49	0.04	0.29	0.02	0.87	0.06	12.8	0.5	14.7	1.1
A ^b	13.55	0.09	0.03	0.47	0.03	0.28	0.02	0.84	0.05	20.9	0.8	24.8	1.8
L ^b	19.78	0.10	0.03	0.45	0.03	0.29	0.02	0.85	0.06	37.7	1.3	44.6	3.5
S ^b	26.14	0.06	0.02	0.36	0.03	0.18	0.01	0.60	0.04	37.7	1.3	62.7	4.08
MAL1	32.46	0.18	0.06	0.46	0.02	0.37	0.01	1.01	0.07	103	3	102	8
MAL13	36.60	0.24	0.09	0.64	0.03	0.53	0.02	1.41	0.09	177	6	125	9
MAL23	40.10	0.23	0.08	0.63	0.03	0.51	0.02	1.36	0.09	154	5	113	8
MAL2	43.61	0.22	0.08	0.56	0.02	0.45	0.02	1.22	0.08	175	6	143	11
MAL14	48.09	0.25	0.09	0.68	0.03	0.53	0.02	1.46	0.10	210	7	143	11
MAL24 ^c	51.90	0.24	0.08	0.72	0.03	0.54	0.02	1.49	0.09	405	14	272	19
MAL3 ^c	57.30	0.24	0.09	0.83	0.04	0.60	0.02	1.66	0.10	409	14	246	17
MAL15 ^c	60.09	0.23	0.08	0.85	0.04	0.59	0.02	1.67	0.10	387	14	232	16
MAL25	64.93	0.33	0.12	0.83	0.04	0.65	0.03	1.81	0.13	337	12	186	15
MAL4	70.07	0.17	0.06	0.47	0.02	0.38	0.02	1.03	0.07	192	6	186	14
MAL16	72.64	0.17	0.06	0.55	0.03	0.41	0.02	1.14	0.07	203	7	179	12
E	74.43	0.22	0.08	0.60	0.05	0.46	0.04	1.27	0.11	355	11	279	25
MAL26	80.43	0.20	0.07	0.63	0.03	0.47	0.02	1.29	0.08	311	12	240	17
MAL5	83.86	0.23	0.08	0.64	0.03	0.50	0.02	1.37	0.09	314	11	229	17
MAL27	89.15	0.28	0.10	0.74	0.03	0.57	0.02	1.58	0.11	403	15	255	20
MAL6	91.99	0.23	0.08	0.68	0.03	0.53	0.02	1.44	0.09	410	15	284	21
MAL17	96.50	0.23	0.08	0.73	0.03	0.54	0.02	1.50	0.09	419	15	280	20
MAL28	101.05	0.17	0.06	0.51	0.02	0.39	0.02	1.08	0.07	283	5	262	19
MAL7	104.37	0.21	0.08	0.56	0.02	0.46	0.02	1.23	0.08	302	10	245	18
MAL29	107.09	0.20	0.07	0.57	0.03	0.44	0.02	1.21	0.08	311	11	257	19
$\mathbf{P}^{\mathbf{c}}$	110.75	0.16	0.06	0.65	0.06	0.44	0.04	1.25	0.09	542	18	432	35
MAL18 ^d	115.23	0.23	0.08	0.74	0.04	0.53	0.02	1.50	0.09	516	19	345	25
MAL8	118.54	0.22	0.08	0.65	0.03	0.49	0.02	1.36	0.09	454	17	333	24
MAL31 ^d	123.49	0.23	0.08	0.72	0.03	0.53	0.02	1.48	0.09	527	20	357	26
MAL19	126.75	0.21	0.07	0.60	0.03	0.46	0.02	1.27	0.08	392	14	309	23
MAL9	130.71	0.18	0.06	0.47	0.02	0.38	0.02	1.03	0.07	314	11	304	23
MAL32	135.13	0.24	0.09	0.64	0.03	0.51	0.02	1.40	0.10	489	18	350	27
MAL20 ^d	138.70	0.23	0.08	0.74	0.03	0.54	0.02	1.51	0.09	602	23	399	29
MAL10 ^d	142.74	0.20	0.07	0.61	0.03	0.47	0.02	1.28	0.08	558	21	436	32
MAL33	146.72	0.17	0.06	0.51	0.02	0.39	0.02	1.07	0.07	414	15	385	28
MAL21	151.11	0.20	0.07	0.54	0.02	0.43	0.02	1.17	0.08	494	18	423	32
MAL11 ^d	154.78	0.22	0.08	0.75	0.04	0.54	0.02	1.51	0.09	615	24	408	29
MAL34 ^d	157.87	0.22	0.08	0.69	0.03	0.51	0.02	1.42	0.09	642	25	451	33
MAL22 ^d	162.49	0.24	0.09	0.69	0.03	0.53	0.02	1.46	0.09	632	25	432	33
MAL12 ^d	164.90	0.21	0.07	0.67	0.03	0.49	0.02	1.36	0.08	597	23	438	31

a Dose rates after correction for water content and, where relevant, attenuation due to grain-size, and an alpha efficiency of 0.04 0.02 (Rees-Jones, 1995).

0.02 are used for quartz and feldspar, respectively (Rees-Jones, 1995). The a-value defines the efficiency with which energy imparted to a crystal by alpha irradiation results in trapped electrons and therefore luminescence. This efficiency is lower for alpha particles than other forms of radiation, since local saturation of electron traps occurs along the alpha track length. However, the a-value must decrease with increasing prior dose, since an alpha track through a region with no trapped electrons will be more efficient at trapping electrons than one through a region where a proportion of the traps are already occupied. Consequently, the a-value varies from a maximum in an unirradiated material, to zero in a saturated material. Rees-Jones (1995) measured a-values for low-dose samples (10 Gy) and hence their values are assumed to represent the maximum for each mineral type. Dated quartz samples presented in this study have equivalent doses 40 Gy, well below the saturation dose for this mineral. Consequently, Rees-Jones s a-value of 0.04 0.02 is appropriate, not least because it is consistent with zero (saturation) at two standard errors. Conversely, all the feldspar samples reported here yield equivalent doses 100 Gy, with the majority between 200 and 700 Gy. Using the natural dose response curve curve (NDRC) defined in section 4.2, the mean NDRC value was calculated every 100 Gy from 200 to 700 Gy, and expressed as a proportion of the saturation level. An age-appropriate a-value was then calculated for each dose by scaling the 0 Gy value (assumed to be 0.86 0.02) by the proportion of saturation, yielding a mean value of 0.04. This mean value, with an appropriately large standard error (0.04 0.02) was used for all feldspar samples, to avoid incorporating an age dependence into the age calculation. This value is consistent at one standard error with all calculated a-values for samples with equivalent doses between 200 and 700 Gy, and at two standard deviations with both saturation and an equivalent dose of \sim 40 Gy.

3.3. Sample preparation

The core is dominated by the silt and clay size sediment fraction with little sand. As such, all dating was done on the 4 11 $\,$ m size fraction. Samples were treated with Na₄P₂O₇ to prevent flocculation, then the fine silt size fraction was isolated using Stokes settling in deionized water. The organic and carbonate components were removed using simultaneous treatment with 30% H₂O₂ and 10% HCl, respectively. Samples were treated until the reaction stopped and were then rinsed three times in deionized water. Quartz-rich samples were produced by

 $^{^{\}rm b}$ Ages based on quartz measurements; all others are based on feldspar.

^c Dates representing reworked material that were removed from the age model.

^d Dates with equivalent doses 500 Gy included in the age model as minimum ages.

treating the resulting polymineral fraction with 35% H₂SiF₆ to remove feldspar grains. Samples were placed in H₂SiF₆ for 96 h, after which they were rinsed three times in deionized water and subsequently immersed in 10 % HCl for 12 h to remove fluoride precipitates. The resulting material was rinsed three times in deionized water and subsequently resettled to 4 m to remove partially dissolved grains. H₂SiF₆ was presaturated with silica by adding an excess of Honeywell 210 300 m silicon dioxide upon purchase. Silicon dioxide was removed immediately prior to use with gravity filtration through Whatman 542 filter paper. Samples were deposited from suspension onto aluminum discs via drying at 50 C. Sufficient sample was added to each drying vessel to produce a monolayer of material on the disc; the sample volume required to achieve this result was estimated by eye. A small number of test discs were measured to establish the approximate equivalent dose for each sample. The youngest four samples were measured using the single-aliquot regenerative-dose technique (SAR) (Murray and Wintle, 2000) applied to quartz separates. All other samples were measured using the polymineral fraction measured with a post-infrared, infrared-stimulated luminescence (pIRIR) measurement sequence (Thomsen et al., 2008). This latter approach is generally considered to yield luminescence ages from the feldspar component of the polymineral fraction.

3.4. Equivalent dose measurements

All luminescence measurements presented in this study were carried out using one of three Ris TL/OSL-DA-20 automated dating systems (B tter-Jensen et al., 2003). Stimulation was carried out using blue (470 nm) or IR (870 nm) light emitting diodes (LEDs) for quartz and polymineral separates, respectively. Luminescence was detected using Electron Tubes Ltd 9235QB15 photomultiplier tubes shielded by Hoya U-340 filters when measuring quartz and Schott BG3 and BG39 filters when measuring polymineral samples. Irradiation was carried out using a 1.48 GBq 90Sr/90Y beta source calibrated relative to the National Physical Laboratory, Teddington ⁶⁰Co -source (Hotspot 800) following Armitage and Bailey (2005). Optimal measurement conditions for both mineral fractions were established using dose recovery tests (Roberts et al., 1999). In the case of quartz, the natural signal was removed using two 200 s room temperature blue diode bleaches separated by a 10 ks pause (Murray and Wintle, 2003), whereas polymineral aliquots were subject to a 48-h exposure in a Dr Honle UVACUBE 400 solar simulator. The single-aliquot regenerative dose technique (Murray and Wintle, 2000) was used to measure the equivalent dose for each fine-grained quartz aliquot presented in this study, while a pIRIR protocol modified from Thomsen et al. (2008) and Li et al. (2014) was applied to polymineral fine-grain aliquots. Equivalent dose (De) measurement procedures for quartz (Table 1a) and polymineral (Table 1b) samples are presented in Table 1.

Quartz dose recovery tests were performed on two aliquots each of the six blind trial samples using the measurement sequence outlined in Table 1a and a known dose of 50 Gy. Dose recovery ratios (measured/ given) were 0.99 0.01, 0.98 0.02, 0.98 0.02, 1.05 0.01, 0.97 0.02 and 1.01 0.01 for samples S, A, M, P, L and E, respectively. In addition, dose recovery experiments were performed, measuring three aliquots at eight different preheat regimes for samples MAL1 (given 60 Gy) and MAL23 (given dose 130 Gy). In the first seven regimes, preheat 1 temperature was varied between 160 and 280 C at 20 C intervals, held for 10 s, all with a 160 C preheat 2 (held for 0 s for preheat 1 temperatures of 160 and 180 C and 5 s for higher temperatures). In addition, a regime using a 260 C preheat 1 and 220 C preheat 2, both held at temperature for 10 s, was also tested. For both samples, aliquots subject to preheat 1 temperatures between 220 and 260 C yielded dose recovery ratios consistent with unity. pIRIR₂₂₅ dose recovery experiments were carried out on three aliquots of each of blind test samples A, S, L and E, using known doses of 51, 60, 64 and 306 Gy respectively. Measurements were performed using the measurement sequence outlined in Table 1b and yielded dose recovery ratios (measured/given) of $1.01 \quad 0.01, \, 0.98 \quad 0.05, \, 0.97 \quad 0.01$ and $0.98 \quad 0.02$ for samples A, S, L and E, respectively, after subtraction of a residual dose of $0.92 \quad 0.16$ Gy.

3.5. Anomalous fading

Infrared-stimulated luminescence signals from the polymineral fraction of sediment are assumed to be dominated by feldspar. Age underestimations caused by anomalous fading are a common problem in feldspar dating and have prevented feldspar dating from reaching widespread application until recently (Wintle, 1973; Huntley and Lamothe, 2001; Thomsen et al., 2008; Roberts et al., 2018). Over the last decade, considerable advances have been made in isolating signals with low fading rates from feldspars by applying an initial low temperature infrared (IR) stimulation followed by a higher temperature IR stimulation (e.g. Thomsen et al., 2008; Li et al., 2014). Using this approach (Table 1b) yielded a mean g-value (i.e. fading rate) for the pIRIR₂₂₅ signal of 0.90 0.39 %/decade (n 33, 3 aliquots each of 11 samples). The tested samples (Mal 1, 2, 15, 16, 27, 28, 18, 19, 20, 21, and 12) were distributed throughout the luminescence dated interval. A dose of ~46 Gy was used for all samples and three measurements were made per aliquot per fading time, with fading durations of 0, 1, 10 and 100 h. Fading rates were determined following Huntley and Lamothe (2001) and Auclair et al. (2003) using Analyst 4.31.9 (Duller, 2015). The measured pIRIR signal g-value from polyminerals is considered low enough to not require fading correction, being similar to the published values obtained for quartz, which is typically considered not to fade. These published quartz fading rates of ~1%/decade (Buylaert et al., 2012) are thought to be a laboratory artifact rather than an indication of true fading; as such it is common practice not to correct for felspar fading rates of 1.5%/decade (Roberts et al., 2018; Buylaert et al., 2013; Feng et al., 2022).

The degree of fading can vary between different forms of feldspar. Feldspars that form under high temperature volcanic settings are known to have more disordered crystal lattices leading to increased rates of fading (Bosken and Schmidt, 2020). While there is volcanism in the East African Rift System, it is dominantly in the eastern branch far from our core site (Biggs et al., 2021). We did not determine the form of feldspar in the samples, but we expect to find few high temperature feldspars. The lake catchment is underlain by Proterozoic rock and the volcanoes nearest to our core site are in the Rungwe volcanic province ~300 km to the north (Fontijn et al., 2010; Fritz et al., 2013). There is little volcanic ash in the core and the few visible tephra that are present are mostly 1 cm thick. The relative absence of high temperature volcanic feldspars reduces the risk of increased feldspar fading rates within our sample set.

3.6. Water content

Water content is a necessary part of luminescence age calculations, with a 1% change in water content yielding a \sim 1% change in dose rate and therefore a ~1% change in calculated age (Roberts et al., 2018). Water content was not measured for these cores until several years after collection, during which time the samples likely experienced differential drying, with both storage conditions and sediment composition impacting drying rates (Bennett et al., 1999; Bird et al., 2004). Because we could not directly measure water content, it was calculated using saturated bulk density from Gamma Ray Attenuation Porosity Evaluation (GRAPE), Total Organic Carbon (TOC), and Biogenic Silica (BiSi) from Si and Ti X-Ray Fluorescence (XRF) measurements. Though GRAPE involves exposing sediments to gamma radiation, Couapel and Bowels (2006) showed that that exposure is of such a short duration, that it does not impact luminescence measurements. They estimated that a typical measurement sequence would expose sediments to 1.45 10 6 Gy and that at even 60 times normal exposure, there was no discernible impact on luminescence results.

GRAPE and XRF data were collected at the University of Minnesota Continental Scientific Drilling Facility (University of Minnesota National Lacustrine Core Repository, 1996) when the cores were first described and were obtained from their data repository. Si and Ti XRF data were used to calculate BiSi following the approach of Johnson et al. (2011). TOC data are from Lyons et al. (2015). Most luminescence samples were taken from core GLAD7-MAL05-1B (Tables 2 and 3); where data for 1B was not available, data from the adjacent and overlapping GLAD7-MAL05-1C was used. GRAPE saturated bulk density was collected every ~1 cm, Si and Ti were collected every ~2 cm, and TOC data was collected every ~28.5 cm. All data were linearly interpolated to the GRAPE saturated bulk density sampling rate. Because this methodology produced a high-density data series (36,150 data points) we were also able to calculate rates of dewatering. While luminescence studies tend to ignore dewatering, a detailed analysis is required in our case due to the significant depth of this core. Compression from overlying sediments caused our samples to lose as much as 12% of their surface water content (see fitted lines in Fig. 3c and d). Our pre-dewatering water content calculation is almost identical to that of Lukas et al. (2012), except that they did not account for BiSi and TOC. They found that their calculations tended to overestimate water content and that the difference increased with increasing water content. This effect may be due to omitting less dense constituents from the computations. Removing BiSi and TOC from our calculations results in an increase in calculated water content.

Our dewatering calculations assume that the coring site was submerged for the entirety of the record. Today the coring site is 592 m deep, and it is unlikely that it was exposed for a significant length of time in the last 500 ka. While there is strong evidence for extreme lowstands, with the most severe potentially reducing lake levels by as much as ~600 m (45-69 mblf) (Lyons et al., 2015), there is no evidence of erosional surfaces in the seismic reflection data at the drill site, indicating long term subaerial exposure is highly unlikely (Lyons et al., 2011). Our calculations also assume that the water content of the recently collected core sections is roughly equal to in situ water content, and that the impacts of expansion due to unloading and compaction during drilling are minimal. While some core sections in the record are clearly disturbed, which may impact their water content, these sections were avoided during sampling.

The water content calculations are described in the following six steps.

Calculate density of water at the room temperature when GRAPE data was collected

Because this composite core totals nearly 450 m total length, GRAPE measurements were generated over several weeks, and the room temperature varied from 23 to 30.5 °C. Density of water at the room temperature during measurement was calculated using the equation originally presented in Thiesen et al. (1900) and revisited by Tanaka et al. (2001), although this correction has an inconsequential (<0.1%) impact on the resulting water content.

Density of Water = $(999.97495 * (1-((((Room Temperature + -3.983035)^2) * (Room Temperature + 301.797))/(522528.9 * (Room Temperature + 69.34881)))))/1000.$

Calculate percent mineral grains of dry material

Percent mineral grains was calculated by subtracting TOC% and BiSi % from an assumed 100% mineral grains of dry material, which resulted in an average value of ~70%. We considered adding carbonates to the calculation, but accounting for carbonates bears little impact on water content. Authigenic carbonates have variable densities (~2.6-2.8 g/cm³) all of which are near that of mineral grains (2.65 g/cm³), so adding carbonates has little impact on water content results.

Mineral Grain% = 100 - BiSi% - TOC%

Calculate dry density

Dry density was calculated using BiSi%, TOC%, Mineral Grain%, and established densities for the three components (Johnson et al., 2011).

Dry Density = (BiSi% * 2 g/cm³) + (TOC% * 1 g/cm³) + (Mineral Grain% * 2.65 g/cm^3).

Calculate volumetric water percent

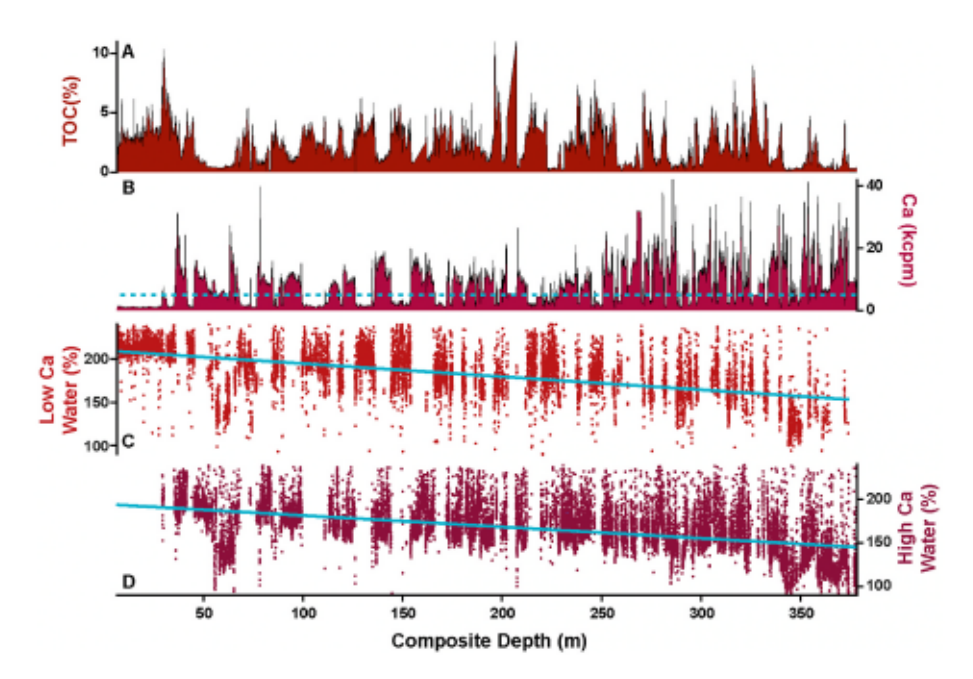


Fig. 3. A: Percent TOC, which has an inverse relationship with Ca throughout the record. B: A 30 point running average of Ca XRF, measured in thousand counts per minute (kcpm). The dividing line between low and high Ca (5 kcpm) is a dotted turquois line. C: The gravimetric water content of low Ca samples, the line of best fit (y = -0.1509x + 209.57), which represents the rate of dewatering, is shown in turquoise. D: The gravimetric water content of high Ca samples, the line of best fit (y = -0.1312x + 194.75), which represents the rate of dewatering, is shown in turquoise. TOC and Ca are from Lyons et al. (2015).

Volumetric Water% was calculated using an equation for calculating porosity from Gealy, 1971). Because the sediments are submerged, all the pore space should be filled and Porosity% should equal to volumetric water%

Volumetrie Water% = ((saturated bulk density - dry density)/(density of water - dry density)) *100.

Convert to gravimetric water percent

While volumetric water content is typically discussed in sedimentological studies, gravimetric water content is specified in the dose rate correction calculations proposed by Aitken (1985, Eq 4.5-4.7) and is used in most luminescence studies. The conversion was made using an equation from Lukas et al. (2012).

Gravimetric water% = Volumetric water% * (dry density/density of water).

Calculate dewatering rate

Calculating dewatering was the most involved step and likely the most novel. The literature on dewatering is limited with few papers in this depth range publishing both water content and a full range of sedimentary characteristics (dry density, TOC, BiSi, carbonate content, grain size, etc.). The studies that are available rarely focus on our depths of interest (0–165 mblf). Bennett et al. (1999) showed a sharp decline in water content in the first few cm after deposition with a leveling off by 5 cm depth. This initial rapid decline will have a negligible impact on our samples as this represents a small portion of our burial history. Bray and Karig (1985) looked at greater depths and found that water content reduces exponentially over several km, with most dewatering occurring in the upper 1.5 km. Burst (1976) argues that in the first 900 m after burial dewatering is driven by gravitational displacement.

Sediment composition and grain size also play an important role in dewatering rates (Bennett et al., 1999; Bird et al., 2004). Grain size tends to impact the compressibility of sediments, with coarser grained sediments having lower water contents at the sediment water interface but dewatering more slowly (Bennett et al., 1999; Bird et al., 2004). Finer grained sediments tend to be both more absorbent and more compressible, with higher water contents observed at the sediment water interface but dewatering more quickly (Bennett et al., 1999; Bird et al., 2004). Sediments with high TOC tend to exhibit higher dewatering rates, with the size of organic fragments also playing a role (Bennett et al., 1999; Bird et al., 2004).

Given the role of sediment type on dewatering rates, an initial attempt was made to base dewatering rates on dry density, wherein a dry density range was set for each sample, and then sediments within that range were identified moving down core. This method, however, produced highly variable dewatering rates, and required that there be sediment with lithology comparable to each luminescence sample at several intervals down core, which is not the case for every sample. Instead, we assume that dewatering rates are approximately linear, and we generate two equations for dewatering for the two dominant lithology types in the core. While dewatering may be exponential at cm and km scales, a linear curve seems to be the best fit on the scale of tens of meters examined here (Fig. 3).

The two dominant sediment types are defined by XRF values for Ca, with high Ca >5000 counts per second and low Ca <5000 counts per second. The Ca record is highly rectified and indicates clear and rapid transitions in Ca throughout the core (Lyons et al., 2015) (Fig. 3b). Transitions are commonly observed at the cm scale and there are few intermediate lithologies. 5000 counts per second was selected as the demarcation between high and low Ca, because it falls between the baseline value of ~2000 counts per second and the minimum height of Ca peaks, ~8000 counts per second. Previous work on this core interprets Ca as an indicator of carbonate content and lowered lake level (Scholz et al., 2007; Lyons et al., 2015). Ca is related to water content in

part because it is inversely related to TOC. While down-core TOC can also be used to demarcate dewatering rates, it does not demonstrate such sharp transitions and there are more sections with intermediate TOC values. It is possible that because Ca is interpreted to vary with lake level, changes in Ca are coeval with changes in grain size. As a coarse and incompressible fraction, carbonates may also behave like siliciclastic sand grains in a dewatering context.

To calculate dewatering rates for the core, all the gravimetric water content data calculated during steps 1–5 were categorized as either high or low Ca sediment. The two resulting datasets were then plotted versus depth and linear lines of best fit were generated. The resulting line of best fit equations are:

y = -0.1312x + 194.75 for high Ca samples

y = -0.1509x + 209.57 for low Ca samples.

The slope of each line is taken as the percent gravimetric water content lost per meter of overlying sediment. The dewatering corrected water content of each sample was calculated by creating a series of test age models to estimate what percentage of the total burial period each sample spent at depths arrayed at 10 cm intervals moving up-core. The dewatering corrected water content was then taken as the temporal mean of water content during the entire burial period. While not computationally complex, these equations effectively reproduce calculated water content at given depths. They also produce water contents of surface sediments with no trend linked to burial depth. These dewatering equations are internally consistent for this location and may be applicable to other settings with different sediment types.

4. Results and discussion

4.1. Blind trial

In the initial phase of this project, we conducted a blind trial to ensure that luminescence dating was feasible for this record. Four of the samples fall in the portion of the record well-dated by ¹⁴C, and two are from deeper in the core. These samples are identified as M, A, L, S, E, and P. The youngest four ages, all based upon quartz, are consistent with the previously published ¹⁴C dates and the identification of the Youngest

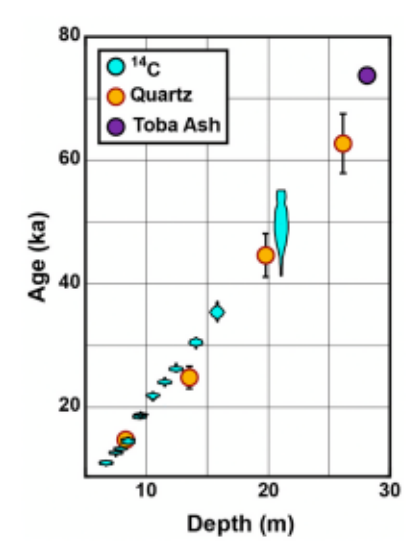


Fig. 4. The youngest four ages, all based on quartz, plotted with the previously published ¹⁴C ages and the identification of the youngest Toba Tuff (Scholz et al., 2007; Lane et al., 2013; Mark et al., 2017). The ¹⁴C ages were calibrated and plotted using the 'draw.dates' function in the R package IntCal (Reimer et al., 2020). The variable width of each ¹⁴C marker represents relative uncertainty, with wider sections of the marker indicating more likely ages. Uncertainties for the youngest luminescence age and the Youngest Toba Tuff are obscured by the marker.

Toba Tuff (Fig. 4). These four represent the only quartz ages used in this study, because quartz reaches saturation well before feldspar, limiting its use to young samples (Buylaert et al., 2012; Arnold et al., 2015). The two older blind trial samples fell within the poorly dated interval of interest. The older of the two, Sample P, had an equivalent dose of 500 Gy and was later removed, as discussed in the following section. The younger sample, Sample E, has an age near that of the existing age models (E 279 25 ka, Lyons 244.5 ka). The results of the blind trial indicated that luminescence dating was reliable at this site and that a larger dating study was appropriate.

4.2. Defining luminescence signal saturation

Using pIRIR measurements, luminescence dating is routinely applicable to ~300 ka in some environments, with some studies demonstrating accurate results beyond this age (Arnold et al., 2015; Fu et al., 2017). In common with all luminescence dating techniques, the upper age limit of the pIRIR method is dependent upon both the maximum equivalent dose which can be accurately measured and the environmental dose rate, since ages are calculated as age equivalent dose/environmental dose rate. The dose rate is an inherent property of any given sample, so the upper age limit of the technique is determined by the maximum absorbed natural radiation dose which can be accurately measured. In all SAR measurement procedures (Murray and Wintle, 2000), natural or regenerated signals (denoted L_n and L_x respectively) are normalized by the response $(T_n$ or $T_x)$ to a fixed laboratory-administered 'test dose, used to monitor and correct for changes in luminescence output per unit dose (sensitivity) which might occur during a measurement sequence. In this study, samples decreased in sensitivity by up to 30% during the course of a measurement sequence. Sensitivity-corrected luminescence intensities are therefore expressed as ratios i.e. L_n/T_n for the natural luminescence intensity and L_x/T_x for regenerated luminescence intensities.

In a typical measurement sequence, the natural luminescence intensity (L_n/T_n) is first measured and then the aliquot is given a number of progressively larger laboratory radiation doses, allowing the luminescence dose response curve (growth curve) to be defined by fitting the resulting range of L_x/T_x values. The equivalent dose for each aliquot is then calculated by interpolation using this curve fit. However, this approach only yields accurate results when the luminescence intensity for a laboratory administered dose (L_x/T_x) is indistinguishable from the luminescence intensity measured for the same dose absorbed during burial, i.e. the growth curve measured in the laboratory must accurately reflect signal growth during irradiation in nature. Chapot et al. (2012) tested this assumption by constructing a natural dose response curve (NDRC) from the L_n/T_n values obtained from a range of known-age loess samples and comparing it to a laboratory dose response curve (LDRC) constructed using laboratory irradiation. They demonstrated that at low doses the NDRC and LDRC were acceptably similar, but at higher doses $L_{\mbox{\scriptsize x}}/T_{\mbox{\scriptsize x}}$ values were larger than $L_{\mbox{\scriptsize n}}/T_{\mbox{\scriptsize n}}$ values for the same dose. In the absence of confounding factors, this discrepancy will lead to underestimation of the equivalent dose and consequently an underestimation of the age. Therefore, the maximum accurate De that can be determined is defined by the dose at which the NDRC and LDRC diverge to an unacceptable degree, however that is defined. Following the approach of Chapot et al. (2012) an NDRC and LDRC were constructed for Lake Malawi. The LDRC was constructed by fitting a general order kinetic model (GOK) (Guralnik et al., 2015) to all regenerated polymineral luminescence intensities produced in this study (n 944), excluding repeat points for any given aliquot. All data were normalized to test dose size (i.e. $(L_x/T_x)^*T_d$ where T_d is the test dose in Gy) to account for variation in test dose size between samples, test doses ranged from 41.6 Gy to 49.9 Gy (Roberts and Duller, 2004). Construction of an NDRC requires that a number of known age samples are available, covering the dose range being studied. The burial dose (Gy) acquired in nature by each sample is then calculated as the age of the sample (ka) multiplied

by its environmental dose rate (Gy/ka) (Chapot et al., 2012). Fitting a plot of test dose normalized natural luminescence intensity ($(L_n/T_n)^*Td$) against calculated natural dose yields the form of the NDRC.

Chapot et al. (2012) were able to sample known age horizons from a loess-palaeosol sequence to generate their NDRC, while Roberts et al. (2021) used depth in the Chew Bahir drill cores as a proxy for age, allowing them to define the maximum natural dose which could be accurately measured. In the present study, there is some agreement between the luminescence ages and the tuned TEX₈₆ ¹⁸O age model (Johnson et al., 2016). Consequently, we use this age model to provide known ages for our samples, excluding those showing evidence of incomplete signal resetting upon deposition, discussed in the next section. This approach may appear circular, but it should be noted that it is only being used to define the maximum equivalent dose which can accurately be measured. Consequently, while our approach does use the tuned TEX₈₆ ¹⁸O age model for the construction of the NDRC by providing the expected age for the depth of each luminescence sample, the approach did not alter the age of any samples or exclude samples because they were inconsistent with the tuned TEX₈₆ ¹⁸O age model. Both the LDRC and NDRC were fitted using the plot GrowthCurve() function provided in the R package Luminescence (Kreutzer et al., 2012). When making equivalent dose determinations, we used a saturating exponential plus linear fit in Analyst (Duller, 2015), though this means our calculations were made using two different curves, there is no material difference between equivalent dose determinations made using each curve. The ratio of equivalent doses calculated using the GOK and saturating exponential plus linear fit for our samples is 0.996 meaning that the GOK value is on average 0.4 0.1% lower than the saturating exponential plus linear fit value. The two different methods were used, because we could not produce the LDRC and NDRC in Analyst.

Having constructed the NDRC and LDRC (Fig. 5a), the discrepancy between the true burial dose in nature and the laboratory equivalent dose calculated using the LDRC was assessed. For doses in the range 20 680 Gy, the LDRC luminescence intensity and dose needed to produce an identical luminescence intensity on the NDRC were calculated. The LDRC:NDRC ratio is the proportional error of an equivalent dose calculated by interpolating an L_n/T_n value drawn from the NDRC onto the LDRC. The slight equivalent dose overestimates ($\sim\!5\%$) at doses below $\sim\!200$ Gy, where the LDRC would be expected to closely resemble the NDRC, implies that the latter is a close but imperfect approximation of the true natural dose response curve. This could be because the data defining the NDRC is more scattered than that defining the LDRC, implying that at all doses Ln/Tn are not solely determined by modelled absorbed dose (i.e. known age * dose rate). Consequently, small variations between the NDRC and LDRC are to be expected.

It is noteworthy that the pronounced dose underestimates noted at higher doses (~500 Gy) in this polymineral fine grain dataset is consistent with the pattern observed by Chapot et al. (2012) for quartz. This analysis demonstrate that high calculated equivalent doses are likely to substantially underestimate the true burial dose in nature, yielding age underestimates. For the purposes of this study, we regard an equivalent dose underestimate that is sufficient to yield an age underestimate greater than the typical 2 uncertainty on our ages, as being unacceptable. The mean 2 uncertainty on our ages is $\sim 15\%$ and a ~15% equivalent dose underestimate occurs at 510 520 Gy (Fig. 5b). Consequently, samples yielding equivalent doses 500 Gy, are included in the age model presented below as minimum age estimations. These samples are indicated in Table 3 and include, Mal18 115.2 mblf, Mal31 123.5 mblf, Mal20 138.7 mblf, Mal10 142.7 mblf, Mal11 154.8 mblf, Mal34 157.9 mblf, Mal22 162.5 mblf, and Mal12 164.9 mblf. Sample P (110.7 mblf), had an equivalent dose 500 Gy and was excluded from the age model as it likely represents reworked material, as explained in the next section.

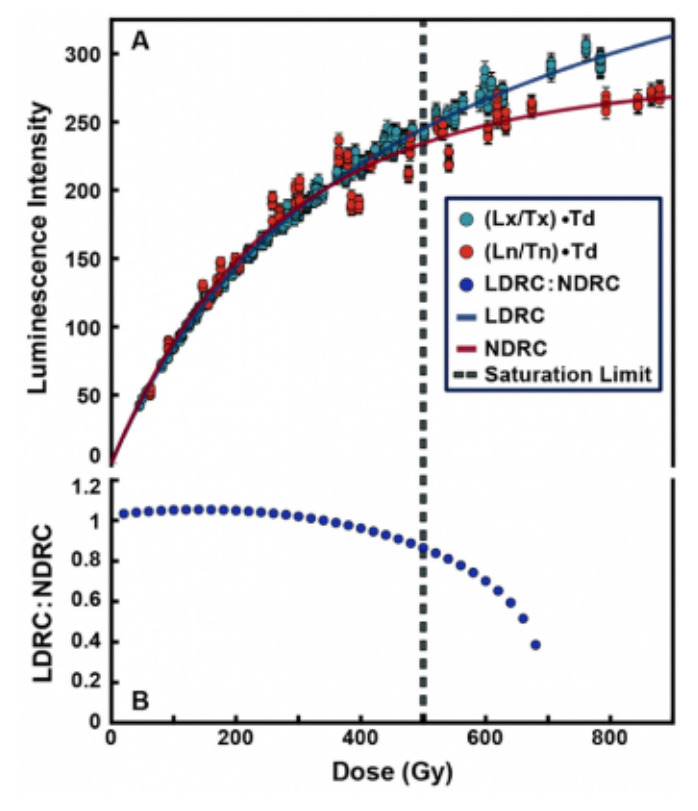


Fig. 5. A: The natural dose response curve (NDRC) based on the Johnson et al. (2016) age model (light blue points and line) compared to the laboratory dose response curve (LDRC) (red points and line). The saturation limit at 500 Gy, which marks the point where the two curves diverge to an unacceptable degree and after which all ages are treated as minimums, is indicated with a gray dashed line. B: The ratio of LDRC to NDRC, indicated with dark blue points. Only the polymineral samples were included in the construction of the LDRC.

4.3. Age overestimation due to subaqueous reworking of sediments

One necessary condition for the production of accurate luminescence ages is that any previous luminescence signal is removed prior to the deposition event that will subsequently be dated. While the pIRIR signal drops rapidly in the first few hours of sunlight exposure, it may require several days of exposure for complete removal of the signal (Colarossi et al., 2015; Smedley and Skirrow, 2020). If there is insufficient sunlight exposure prior to burial, the sample will retain signal relating to previous radiation exposure and therefore the equivalent dose will be larger than the dose absorbed during the most recent burial period. The situation is often referred to as incomplete or partial-bleaching and results in age overestimation. Four samples yield ages which are between 46 and 175 ka older than their nearest neighbors (Mal24, Mal3, Mal15, and P) (Fig. 6). These samples were prepared in different batches and were

measured in separate measurement sequences, implying that contamination, instrumental error, and user error are unlikely to account for the age discrepancy. The four samples are all from laminated sections of the core precluding the possibility of large-scale slumping or turbidites (Fig. 6). Further, seismic imagery from the core site shows no evidence of large-scale displacement or overturning of sediments (Figure B1) (Lyons et al., 2011).

Samples Mal24, Mal3, and Mal15 occur in succession (52-60 mblf) and were deposited during an interval interpreted as extremely arid, where the lake's water volume reduced by at least 95% (Cohen et al., 2007; Scholz et al., 2007; Lyons et al., 2015). During lowstands, lake sediment which had previously been deeply submerged may become prone to reworking by near surface subaqueous processes such as wave action (Verschuren, 1999; Filippi and Talbot, 2005). Since water rapidly attenuates sunlight, this reworking could result in the introduction of resuspended fine-grained sediment to the water column, without that material having been exposed to sufficient sunlight to reduce the luminescence signal. Consequently, sedimentation at the core site would consist of a mixture of a contemporaneous component (zero luminescence age upon deposition) and a component retaining a luminescence signal accumulated during the previous period of burial. The 4-11 um size fraction, studied here, may be especially prone to this, as the fine particles can be transported long-distances to the core site while still producing a laminated sediment. This process may account for the stratigraphic reversal seen in the ages for Mal 24, Mal 3, and Mal 15. The degree to which the luminescence ages overestimate the timing of sedimentation will depend upon both the proportion of the sediment derived from reworking and the equivalent dose of the material being

While sample P is not interpreted to have been deposited during a lowstand, there is evidence from diatom samples that it also contains reworked material. The diatom assemblage nearest to sample P (5 cm below), is made up of 46% benthic taxa including 27% Epithemia sp. This assemblage is unlike that of the neighboring samples, 10 cm up and down core, which contain few Epithemia and 28% and 5% benthic taxa respectively. Given the water depth, it is unlikely that benthic taxa lived at the core site, and rather they were likely carried in (Haberyan and Mhone, 1991). The dominant Epithemia in the sample nearest P is large, ~30 µm long, and heavily silicified, suggesting it would require greater wave energy for transport than the more common small Fragilaria found at this site (Stone et al., 2011). Long distance transport of benthic taxa is a regular process in Lake Malawi (Gasse et al., 2002; Stone et al., 2011), but the sudden increase and large size of the species make small-scale slumping or shoreline erosion reasonable assumptions (Haberyan and Mhone, 1991).

To test for the presence of partially-bleached samples in our dataset, we plotted IR₆₀ equivalent doses against the pIRIR₂₂₅ doses for all the Lake Malawi samples (Fig. 7) (Buylaert et al., 2013; Roberts et al., 2018). IR₆₀ equivalent doses were calculated using data collected during the pIRIR₂₂₅ measurement sequence (Table 1b). Initially, all data were fitted with a general order kinetic model (Guralnik et al., 2015)

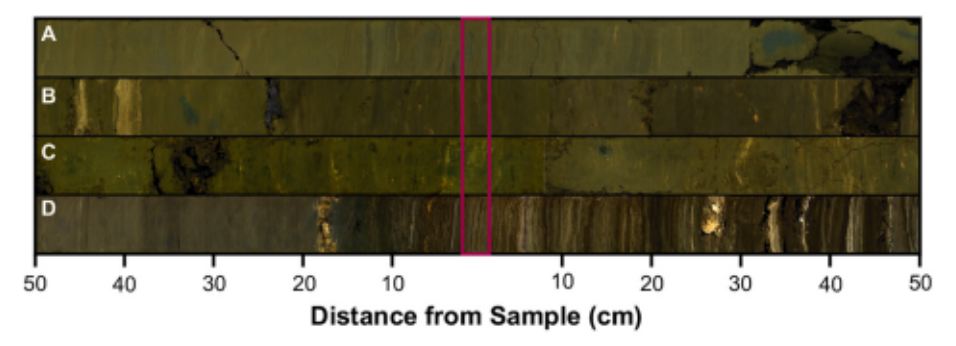


Fig. 6. Core images for partially bleached samples. Sampled section highlighted in red. A: Mal 24 B: Mal 3 C: Mal 15 D: P.

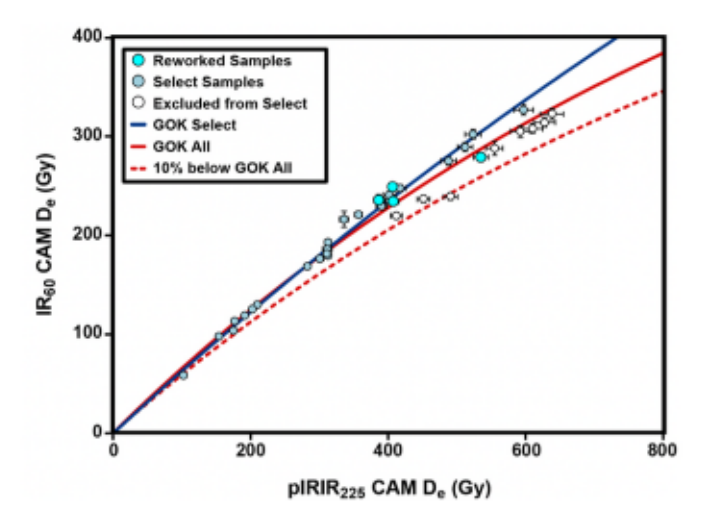


Fig. 7. IR₆₀ equivalent doses plotted against pIRIR₂₂₅ doses. All equivalent doses were calculated using the Central Age Model. Individual data points are shown with 1 standard error uncertainties. Blue solid line: General order kinetic fit through selected (pale blue) data points. Red solid line: General order kinetic (Guralnik et al., 2015) fit through all datapoints. Red dashed line: 10% below the fit through all data points. Light blue symbols represent data included in both fits; white symbols were excluded from the fit through selected points. Bright blue symbols represent samples excluded from the age model due their apparent overestimation of the age of deposition. Of these points, the three clustered around a pIRIR₂₂₅ De of ~400 Gy (MAL3, 15 and 24) were included in both fits, the sample ~535 Gy (P) was excluded from the fit through selected points.

represented by a solid red line in Fig. 7. Samples lying below (to the right of) this line may be partially bleached, since the pIRIR₂₂₅ signal is reduced by sunlight exposure more slowly than the IR₆₀ signal. Buylaert et al. (2013) rejected all data that lay more than one standard deviation below a line that was 10% below a smooth fit to their selected data. Although arbitrary, their approach provides a mechanistic test by which to exclude samples which may be partially bleached. None of the Lake Malawi samples fail this test, implying that no or at least negligible partial bleaching is apparent in this dataset. Though MAL21 is below the 10% line, it is not more than one standard deviation below the line (dashed red line).

It is notable, however, that while no samples fail this test as outlined, there is some spread to the data. Visual inspection suggests that most of the samples lie on a single curve, with 9 samples (white symbols) below it. When a curve is fit to all but these 9 samples (blue line), MAL21 lies more than one standard deviation below a line 10% below this curve and MAL22 is below the 10% line but within one standard deviation of it. All other samples lie within 10% of the fit to the selected data. This analysis implies that partial-bleaching is largely absent from the Lake Malawi dataset, with only MAL21 failing the test proposed by Buylaert et al. (2013), and then only when an arbitrary selection of the data is made. Consequently, no samples were excluded from the age model due to partial-bleaching. The samples identified as potentially yielding age overestimates (bright blue symbols) have IR60/IR225 ratios consistent with the rest of the dataset. We conclude that these samples contain grains that were fully bleached when deposited, meaning that partial-bleaching does not explain their apparently anomalous ages. Instead, we propose that all the constituent grains within these samples were fully bleached prior to initial deposition, but some proportion of them were subaqueously reworked, without sunlight exposure, and hence were deposited at the core site with a substantial luminescence signal relating to prior burial.

To test the influence that the potentially reworked samples (Mal24, Mal3, Mal15, and P) would have on the age model, we ran two versions, one that includes these samples and one that excludes them. Bayesian

models will often exclude outliers on their own, eliminating the need to remove dubious ages. This is most likely to occur when there are few outliers, not like the three in a row that we see. Including the potentially reworked ages in the model had a modest impact, with the age model largely aligning with the younger ages that show no signs of reworking. In the section of the core surrounding Mal24, Mal3, and Mal15 and the section surrounding sample P, the age model that included the potentially reworked samples was on average ~ 15 ka and ~ 5 ka, respectively, older than the age model that did not include the potentially reworked samples. In the age model that included the potentially reworked samples, all four had their full 26 uncertainty fail to overlap with the 95% confidence interval of the model. The mean difference between the maximum age of the 95% confidence interval at the depth of each sample and the minimum 20 uncertainty of each was ~40 ka. Given that Mal24, Mal3, Mal15, and P lie in sections of the core where we would expect to find reworked sediments and because the Bayesian model sees the ages as improbable, we determined that the most conservative approach was to exclude these samples from the final age model.

4.4. Age model

The age model was generated using the Bayesian-based program Bacon (Fig. 8, Figure B2) (Blaauw and Christen, 2011). While Bacon is typically used on shorter ¹⁴C-dominated records, the fundamental workings do not preclude using other kinds of dates or longer records. It has also been effectively applied to sediment cores within the age range of this record (Owen et al., 2018; Chen et al., 2020). The new age model includes the accepted luminescence dates, the previously published ¹⁴C ages, the Youngest Toba Tuff, Ar-Ar, and paleomagnetic reversal ages (Table B1) (Scholz et al., 2007; Lane et al., 2013; Lyons et al., 2015; Mark et al., 2017; Channell et al., 2020). Though there is some scatter in the luminescence dates, the new dates effectively fill the gap between the youngest Ar-Ar date and the Youngest Toba Tuff.

Within the interval of interest, spanning from the youngest Ar–Ar date at \sim 165 mblf and the Youngest Toba Tuff at \sim 30 mblf, the model generated in this paper falls between the three published age models (Lyons et al., 2015; Ivory et al., 2016; Johnson et al., 2016) and tends to skew to the older end. This places it nearest to the TEX₈₆ δ^{18} O tuned Johnson et al. (2016) model, which itself falls between the often older, linearly interpolated Lyons et al. (2015) model and the often younger,

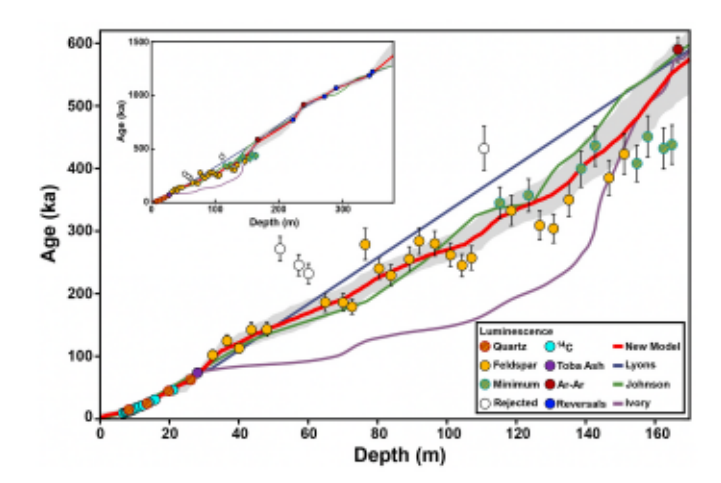


Fig. 8. The age model produced using the R-based Bayesian modeling program Bacon. In addition to our new luminescence dates, the model includes 12 AMS radiocarbon dates (<50 ka), identification of a tephra from the Youngest Toba Tuff (73.7 ka), 2 Ar–Ar dates on tephras (590 and 915 ka), and 5 Paleomagnetic reversals (790–1220 ka) (Scholz et al., 2007; Lane et al., 2013; Lyons et al., 2015; Mark et al., 2017; Channell et al., 2020). The 95% confidence interval for the model is represented by the gray halo. The previously published age models and removed luminescence ages are displayed for reference.

paleomagnetic Ivory et al. (2016) model. While the Johnson et al. (2016) model is younger than the Lyons et al. (2015) model through most of the interval, the models overlap at the start and end of the interval from ${\sim}165$ to ${\sim}150$ mblf and from ${\sim}45$ to ${\sim}30$ mblf. The model generated in this paper generally yields younger ages than the Lyons et al. (2015) model, and is only older than the Lyons et al. (2015) age model in the youngest part of the interval of interest, from \sim 50 to \sim 30 mblf. The difference between these two models is modest at the start and end of the interval of interest, placing the Lyons et al. (2015) age model within the 95% confidence interval of the model presented in this paper from ${\sim}165$ to ${\sim}155$ mblf and from ${\sim}60$ to ${\sim}30$ mblf. In the middle of the interval of interest the difference between the two models expands to ~80 ka, placing the Lyons et al. (2015) age model well outside the 95% confidence interval of the model presented in this paper. From ~ 165 to \sim 95 mblf the Johnson et al. (2016) model tends to be older than the model presented in this paper, at times by as much as 50 ka. At shallower depths the relationship reverses and from ~95 to ~30 mblf the age model presented in this paper is slightly older by 10 20 ka. Throughout most of the interval of interest, the Johnson et al. (2016) age model is within the 95% confidence interval of the age model presented in this paper. Though, as paleoenvironmental data, rightly or wrongly, is often presented only using the median age model there would still be significant differences between data visualized using the two age models. The Ivory et al. (2016) model is characterized by dramatic changes in sedimentation rates, with an interval of exceptionally low sedimentation rates from ~155 to ~140 mblf and an interval of exceptionally high sedimentation rates from \sim 140 to \sim 30 mblf. This trend makes the Ivory et al. (2016) model much younger than and well outside the 95% confidence interval of the age model generated for this paper for most of the interval, the maximum difference between the two models is \sim 140 ka. From ~ 165 to ~ 155 mblf, however, the two age models are in near agreement and the Ivory et al. (2016) age model is well within the 95% confidence interval of the model presented in this paper.

Despite similarities with existing models, the model generated in this paper has great advantage in reducing uncertainty, removing circular reasoning, and recognizing potentially problematic sections of the record. Though none of the published models use techniques that produce a quantitative uncertainty, sparsely dated models like Lyons et al. (2015) require excessive interpolation and tend to have ballooning uncertainty between tie points (Zimmerman and Wahl, 2020). Although this is chronologically justifiable, since age uncertainty does increase with increasing durations of interpolation, this feature hinders comparison with other records. With 35 total luminescence dates, our model largely avoids this issue in our interval of interest. Our model also produces a quantitative uncertainty, which is useful for comparing paleoenvironmental records from different sources. Though the Johnson et al. (2016) model has several tie points in the interval of interest, these are based on tuning. Tuning environmental proxies to produce an age model requires making assumptions about what controls a system. When these environmental proxies and the resulting age model are then used to make interpretations about controls on that same system, a circular argument is produced. In these cases, the age model and resulting interpretations cannot be independently validated, making it difficult to have full confidence in either. The published models are also less likely to perceive disturbed sedimentation and hiatuses. For instance, none of the published age models recognise the reworking of sediment which we hypothesise resulted in age overestimates for samples MAL 24, 3, 15 and P. Missing this disturbance may have led to misidentified paleomagnetic excursions in the Ivory et al. (2016) model. The new luminescence dated model identifies reworking of sediments not visible in the published models, reduces the uncertainties inherent to sparsely dated models, and allows for fully independent assessment of climatic drivers.

5. Conclusion

As the longest most continuous record from the continental tropics,

this drill core from Lake Malawi holds tremendous potential to determine climatic drivers in the region. While much work has been attempted in the nearly two decades since the core was collected, use of the record has been limited by a gap in directly dated sediments, between ~74 ka and ~590 ka (28 167 mblf). Previously published age models attempted linear interpolation between the tie points, identification of paleomagnetic excursions, and tuning to the global ¹⁸O stack. These methods produced contrasting models that cannot be reconciled. Here we use luminescence dating to resolve this long-running issue. Our new model uses direct numerical dating to effectively fill the gap in previously published chronologies for this record, allowing for a reassessment of the regional implications of existing proxy records and for new higher resolution work to be conducted. It may also be feasible to use the new luminescence dates as tie points for other forms of dating. This study adds to the growing body of data that demonstrates that luminescence dating is now well suited for dating lacustrine records in this age range. It also adds to work showing that water content history, necessary for luminescence dating, can be effectively calculated for sediment cores that have been split and stored for many years, using data that is routinely collected during initial core characterization. With proven success, luminescence dating can and should be used to revisit the age models of archived core material and, where needed, to resolve chronologic disputes.

Declaration of competing interest

The authors declare that they have no known competing financial interests or personal relationships that could have appeared to influence the work reported in this paper.

Data availability

The age-depth model output is in Appendix A.

Acknowledgements

Support for this work was provided by a Syracuse University Research Excellence Doctoral Funding Fellowship, a University of Minnesota National Lacustrine Core Repository Visiting Graduate Student Program Grant, the Geological Society of America Continental Scientific Drilling Division, the Syracuse University Department of Earth and Environmental Sciences, a Syracuse University 'Cuse COVID Relief grant, and NSF awards 1449617 (CAS co-PI) and 2116017 (CAS PI). SJA s contribution to this work was partly supported by the Research Council of Norway, through its Centres of Excellence funding scheme, SFF Centre for Early Sapiens Behaviour (SapienCE), project number 262618. We thank T.C. Johnson and S. Ivory for extensive discussions regarding Lake Malawi drill core geochronology, R. Brown and E.T. Brown for assistance with X-ray fluorescence data, and the University of Minnesota National Lacustrine Core Repository for access to cores and stored data. We thank two reviewers who provided numerous constructive criticisms and suggestions that helped to improve the manuscript.

Appendix A. Supplementary data

Supplementary data to this article can be found online at https://doi.org/10.1016/j.quascirev.2024.108691.

References

Aitken, M.J., 1985. Thermoluminescence Dating. Academic Press, London.
 Armitage, S.J., Bailey, R.M., 2005. The measured dependence of laboratory beta dose rates on sample grain size. Radiat. Meas. 39, 123–127.
 Armitage, S.J., Pinder, R.C., 2017. Testing the applicability of optically stimulated luminescence dating to Ocean Drilling Program cores. Quat. Geochronol. 39, 124–130.

L.C. Streib et al.

- Arnold, L.J., Demuro, M., Pares, J.M., Perez-Gonzalez, A., Arsuaga, J.L., Bermúdez de Castro, J.M., Carbonell, E., 2015. Evaluating the suitability of extended-range luminescence dating techniques over early and Middle Pleistocene timescales: published datasets and case studies from Atapuerca, Spain. Quat. Int. 389, 167–190.
- Auclair, M., Lamothe, M., Huot, S., 2003. Measurement of anomalous fading for feldspar IRSL using SAR. Radiat. Meas. 37 (4 5), 487–492.
- Bennett, R.H., Ransom, B., Kastner, M., Baerwald, R.J., Hulbert, M.H., Sawyer, W.B., Olsen, H., Lambert, M.W., 1999. Early diagenesis: impact of organic matter on mass physical properties and processes, California continental margin. Mar. Geol. 159 (1 4), 7 34.
- Berger, G.W., Easterbrook, D.J., 1993. Thermoluminescence dating tests for lacustrine, glaciomarine, and floodplain sediments from western Washington and British Columbia. Can. J. Earth Sci. 30, 1815–1828.
- Berger, G.W., Anderson, P.M., 1994. Thermoluminescence dating of an arctic lake core from Alaska. Quat. Sci. Rev. 13 (5 7), 497 501.
- Berger, G.W., Doran, P.T., 2001. Luminescence-dating zeroing tests in Lake Hoare, Taylor valley, Antarctica. J. Paleolimnol. 25, 519 529.
- Biggs, J., Ayele, A., Fischer, T.P., Fontijn, K., Hutchison, W., Kazimoto, E., Whaler, K., Wright, T.J., 2021. Volcanic activity and hazard in the East African rift zone. Nat. Commun. 12 (1), 6881.
- Bird, M.I., Fifield, L.K., Chua, S., Goh, B., 2004. Calculating sediment compaction for radiocarbon dating of intertidal sediments. Radiocarbon 46 (1), 421–435.
- Blaauw, M., Christen, J.A., 2011. Flexible paleoclimate age-depth models using an autoregressive gamma process. Bayesian analysis 6 (3), 457–474.
- Blaauw, M., Christen, J.A., Bennett, K.D., Reimer, P.J., 2018. Double the dates and go for Bayes impacts of model choice, dating density and quality on chronologies. Quat. Sci. Rev. 188, 58 66.
- Bosken, J.J., Schmidt, C., 2020. Direct and indirect luminescence dating of tephra: a review. J. Quat. Sci. 35 (1 2), 39 53.
- B tter-Jensen, L., Andersen, C.E., Duller, G.A.T., Murray, A.S., 2003. Developments in radiation, stimulation and observation facilities in luminescence measurements. Radiat. Meas. 37, 535–541.
- Bray, C.J., Karig, D.E., 1985. Porosity of sediments in accretionary prisms and some implications for dewatering processes. J. Geophys. Res. 90 (B1), 768 778.
- Brown, E.T., Johnson, T.C., Scholz, C.A., Cohen, A.S., King, J.W., 2007. Abrupt changes in tropical African climate linked to the bipolar seesaw over the past 55,000 years. Geophys. Res. Lett. 33 (20).
- Burst, J.F., 1976. Argillaceous sediment dewatering. Annu. Rev. Earth Planet Sci. 4, 293.
 Buylaert, J.P., Jain, M., Murray, A.S., Thomsen, K.J., Thiel, C., Sohbati, R., 2012.
 A robust feldspar luminescence dating method for Middle and Late Pleistocene sediments. Boreas 41 (3), 435–451.
- Buylaert, J.P., Murray, A.S., Gebhardt, A.C., Sohbati, R., Ohlendorf, C., Thiel, C., Wastegård, S., Zolitschka, B., 2013. Luminescence dating of the PASADO core 5022-1D from Laguna Potrok Aike (Argentina) using IRSL signals from feldspar. Quat. Sci. Rev. 71, 70–80.
- Caley, T., Extier, T., Collins, J.A., Schefu, E., Dupont, L., Malaize, B., Rossignol, L., Souron, A., McClymont, E.L., Jimenez-Espejo, F.J., García-Comas, C., 2018. A twomillion-year-long hydroclimatic context for hominin evolution in southeastern Africa. Nature 560, 76–79.
- Castaneda, I.S., Caley, T., Dupont, L.M., Kim, J., Malaize, B., Schouten, S., 2016. Middle to Late Pleistocene vegetation and climate change in subtropical southern East Africa. Earth Planet Sci. Lett. 450, 306–316.
- Channell, J.E., Singer, B.S., Jicha, B.R., 2020. Timing of Quaternary geomagnetic reversals and excursions in volcanic and sedimentary archives. Quat. Sci. Rev. 228, 106114
- Chapot, M.S., Roberts, H.M., Duller, G.A.T., Lai, Z.P., 2012. A comparison of natural- and laboratory-generated dose response curves for quartz optically stimulated luminescence signals from Chinese Loess. Radiat. Meas. 47, 1045–1052.
- Chen, C.Y., McGee, D., Woods, A., Perez, L., Hatfield, R.G., Edwards, R.L., Cheng, H., Valero-Garces, B.L., Lehmann, S.B., Stoner, J.S., Schwalb, A., 2020. U-Th dating of lake sediments: lessons from the 700 ka sediment record of Lake Junín, Peru. Quat. Sci. Rev. 244, 106422.
- Cohen, A.S., Stone, J.R., Beuning, K.R., Park, L.E., Reinthal, P.N., Dettman, D., Scholz, C. A., Johnson, T.C., King, J.W., Talbot, M.R., Brown, E.T., 2007. Ecological consequences of early Late Pleistocene megadroughts in tropical Africa. Proc. Natl. Acad. Sci. USA 104 (42), 16422 16427.
- Colarossi, D., Duller, G.A., Roberts, H.M., Tooth, S., Lyons, R., 2015. Comparison of paired quartz OSL and feldspar post-IR IRSL dose distributions in poorly bleached fluvial sediments from South Africa. Quat. Geochronol. 30, 233–238.
- Couapel, M.J., Bowles, C.J., 2006. Impact of gamma densitometry on the luminescence signal of quartz grains. Geo Mar. Lett. 26, 1 5.
- Duller, G.A., 2008. Single-grain optical dating of Quaternary sediments: why aliquot size matters in luminescence dating. Boreas 37 (4), 589 612.
- Duller, G.A., 2015. The Analyst software package for luminescence data: overview and recent improvements. Ancient TL 33 (1), 35–42.
- Eccles, D.H., 1974. An outline of the physical limnology of Lake Malawi (Lake Nyasa). Limnol. Oceanogr. 19 (5), 730 742.
- Farr, T.G., Kobrick, M., 2000. Shuttle radar topography mission produces a wealth of data. Eos 81 (48), 583.
- Feng, Y., Hou, Y., Zhang, J., Yang, N., Cai, Y., Yang, F., Gu, J., Long, H., 2022. Timing of Holocene lake highstands around Dawa Co in inner Tibetan Plateau: comparison of quartz and feldspar luminescence dating with radiocarbon age. Quat. Geochronol. 69, 101267.
- Fields, S., 2005. Continental divide: why Africa's climate change burden is greater. Environ. Health Perspect. 113 (8), A534 A537.

- Filippi, M.L., Talbot, M.R., 2005. The palaeolimnology of northern Lake Malawi over the last 25 ka based upon the elemental and stable isotopic composition of sedimentary organic matter. Quat. Sci. Rev. 24 (10 11), 1303 1328.
- Fontijn, K., Delvaux, D., Ernst, G.G.J., Kervyn, M., Mbede, E., Jacobs, P., 2010. Tectonic control over active volcanism at a range of scales: case of the Rungwe Volcanic Province, SW Tanzania; and hazard implications. J. Afr. Earth Sci. 58, 764 777.
- Foerster, V., Asrat, A., Bronk Ramsey, C., Brown, E.T., Chapot, M.S., Deino, A., Duesing, W., Grove, M., Hahn, A., Junginger, A., Kaboth-Bahr, S., 2022. Pleistocene climate variability in eastern Africa influenced hominin evolution. Nat. Geosci. 15 (10), 805–811.
- Fritz, H., Abdelsalam, M., Ali, K.A., Bingen, B., Collins, A.S., Fowler, A.R., Ghebreab, W., Hauzenberger, C.A., Johnson, P.R., Kusky, T.M., Macey, P., Muhongo, S., Stern, R.J., Viola, G., 2013. Orogen styles in the East African Orogen: a review of the Neoproterozoic to Cambrian tectonic evolution. J. Afr. Earth Sci. 86, 65 106.
- Fu, X., Cohen, T.J., Arnold, L.J., 2017. Extending the record of lacustrine phases beyond the last interglacial for Lake Eyre in central Australia using luminescence dating. Quat. Sci. Rev. 162, 88 110.
- Gasse, F., Barker, P., Johnson, T.C., 2002. A 24,000 yr diatom record from the northern basin of Lake Malawi. In: The East African Great Lakes: Limnology, Palaeolimnology and Biodiversity. Springer, Dordrecht, pp. 393 414.
- Gealy, E.L., 1971. Saturated bulk density, grain density, and porosity of sediment cores from the western equatorial Pacific: Leg 7, Glomar Challenger. In: Initial Report of the Deep Sea Drilling Project, 7, 1081-1104.
- Guralnik, B., Li, B., Jain, M., Chen, R., Paris, R.B., Murray, A.S., Li, S.-H., Pagonis, P., Herman, F., 2015. Radiation-induced growth and isothermal decay of infraredstimulated luminescence from feldspar. Radiat. Meas. 81, 224–231.
- Haberyan, K.A., Mhone, O.K., 1991. Algal communities near Cape Maclear, southern lake Malawi, Africa. Hydrobiologia 215 (3), 175 188.
- Huntley, D.J., Lamothe, M., 2001. Ubiquity of anomalous fading in K-feldspars and the measurement and correction for it in optical. Can. J. Earth Sci. 38 (7), 1093 1106.
- Ivory, S., Blome, M., King, J., McGlue, M., Cole, J., Cohen, A., 2016. Environmental change explains cichlid adaptive radiation at Lake Malawi over the past 1.2 million years. Proc. Natl. Acad. Sci. U.S.A. 113, 11895 11900.
- Ivory, S.J., Lezine, A., Vincens, A., Cohen, A.S., 2018. Waxing and waning of forests: late quaternary biogeography of southeast Africa. Global Change Biol. 24 (7), 2939–2951.
- Jacobs, Z., Roberts, R.G., 2007. Advances in optically stimulated luminescence dating of individual grains of quartz from archeological deposits. Evol. Anthropol. 16 (6), 210–223.
- Jain, M., Murray, A.S., Botter-Jensen, L., 2004. Optically stimulated luminescence dating: how significant is incomplete light exposure in fluvial environments? Ouaternaire 15 (1), 143–157.
- Johnson, T.C., Brown, E.T., Shi, J., 2011. Biogenic silica deposition in Lake Malawi, East Africa over the past 150,000 years. Palaeogeogr. Palaeoclimatol. Palaeoecol. 303 (1 4), 103 109.
- Johnson, T.C., Werne, J.P., Brown, E.T., Abbott, A., Berke, M., Steinman, B.A., Halbur, J., Contreras, S., Grosshuesch, S., Deino, A., Lyons, R.P., Scholz, C.A., Schouten, S., Sinninghe Damste, J.S., 2016. A progressively wetter climate in southern East Africa over the past 1.3 million years. Nature 537 (7619), 220 224.
- Kreutzer, S., Schmidt, C., Fuchs, M.C., Dietze, M., Fuchs, M., 2012. Introducing an R package for luminescence dating analysis. Ancient TL 30, 1 8.
- Lamb, H.F., Bates, C.R., Bryant, C.L., Davies, S.J., Huws, D.G., Marshall, M.H., Roberts, H.M., Toland, H., 2018. 150,000-year palaeoclimate record from northern Ethiopia supports early, multiple dispersals of modern humans from Africa. Sci. Rep. 8, 1077.
- Lane, C.S., Chorn, B.T., Johnson, T.C., 2013. Ash from the Toba supereruption in Lake Malawi shows no volcanic winter in East Africa at 75 ka. Proc. Natl. Acad. Sci. USA 110 (20), 8025–8029.
- Lean, J., Beer, J., Bradley, R., 1995. Restructuring of solar irradiance since 1610: implications for climate change. Geophys. Res. Lett. 22 (23), 3195–3198.
- Li, B., Jacobs, Z., Roberts, R.G., Li, S.-H., 2014. Review and assessment of the potential of post-IR IRSL dating methods to circumvent the problem of anomalous fading in feldspar luminescence. Geochronometria 41, 178
- Lukas, S., Preusser, F., Anselmetti, F.S., Tinner, W., 2012. Testing the potential of luminescence dating of high-alpine lake sediments. Quat. Geochronol. 8, 23–32.
- Lupien, R.L., Russell, J.M., Yost, C.L., Kingston, J.D., Deino, A.L., Logan, J., Schuh, A., Cohen, A.S., 2021. Vegetation change in the Baringo basin, east Africa across the onset of northern hemisphere glaciation 3.3 2.6 Ma. Palaeogeogr. Palaeoclimatol. Palaeoecol. 570, 109426.
- Lupien, R.L., Russell, J.M., Pearson, E.J., Castaneda, I.S., Asrat, A., Foerster, V., Lamb, H. F., Roberts, H.M., Schabitz, F., Trauth, M.H., Beck, C.C., 2022. Orbital controls on eastern African hydroclimate in the Pleistocene. Sci. Rep. 12 (1), 3170.
- Lyons, R.P., Scholz, C.A., Buoniconti, M.R., Martin, M.R., 2011. Late Quaternary stratigraphic analysis of the Lake Malawi Rift, East Africa: an integration of drill-core and seismic-reflection data. Palaeogeogr. Palaeoclimatol. Palaeoecol. 303 (1 4), 20, 37
- Lyons, R., Scholz, C., Cohen, A., King, J., Brown, E., Ivory, S., Johnson, T.C., Deino, A., Reinthal, P., McGlue, M., Blome, M., 2015. Continuous 1.3-million-year record of East African hydroclimate, and implications for patterns of evolution and biodiversity. Proc. Natl. Acad. Sci. U.S.A. 112 (51), 15568 15573.
- Mark, D.F., Renne, P.R., Dymock, R.C., Smith, V.C., Simon, J.I., Morgan, L.E., Staff, R.A., Ellis, B.S., Pearce, N.J., 2017. High-precision ⁴⁰Ar/³⁹Ar dating of Pleistocene tuffs and temporal anchoring of the Matuyama-Brunhes boundary. Quat. Geochronol. 39, 1 23.
- Maslin, M.A., Shultz, S., Trauth, M.H., 2015. A synthesis of the theories and concepts of early human evolution. Phil. Trans. Biol. Sci. 370 (1663), 20140064.

- Murray, A.S., Wintle, A.G., 2000. Luminescence dating of quartz using an improved single-aliquot regenerative-dose protocol. Radiat. Meas. 32, 57–73.
- Murray, A.S., Wintle, A.G., 2003. The single aliquot regenerative dose protocol: potential for improvements in reliability. Radiat. Meas. 37, 377–381.
- Owen, R.B., Crossley, R., 1992. Spatial and temporal distribution of diatoms in sediments of Lake Malawi, Central Africa, and ecological implications. J. Paleolimnol. 7, 55, 71
- Owen, R.B., Muiruri, V.M., Lowenstein, T.K., Renaut, R.W., Rabideaux, N., Luo, S., Deino, A.L., Sier, M.J., Dupont-Nivet, G., McNulty, E.P., Leet, K., 2018. Progressive aridification in East Africa over the last half million years and implications for human evolution. Proc. Natl. Acad. Sci. USA 115 (44), 11174 11179.
- Pilskaln, C.H., 2004. Seasonal and interannual particle export in an African rift valley lake: a 5-yr record from Lake Malawi, Southern East Africa. Limnol. Oceanogr. 49 (4), 964–977.
- Prescott, J.R., Hutton, J.T., 1994. Cosmic ray contributions to dose rates for luminescence and ESR dating: large depths and long-term time variations. Radiat. Meas. 23, 497 500.
- Rees-Jones, J., 1995. Optical dating of young sediments using fine-grained quartz. Ancient TL 13, 9 $\,14.$
- Reimer, P.J., Austín, W.E.N., Bard, E., Bayliss, A., Blackwell, P.G., Ramsey, C.B., Butzin, M., Cheng, H., Edwards, R.L., Friedrich, M., Pieter, M Groote, Guilderson, T. P., Hajdas, I., Heaton, T.J., Hogg, A.G., Hughen, K.A., Bernd, K., Manning, S.W., Muscheler, R., Palmer, J.G., Pearson, C., van der Plicht, J., Reimer, R.W., Richards, D.A., Scott, E.M., Southon, J.R., Turney, C.S.M., Wacker, L., Adolphi, F., Büntgen, U., Capano, M., Fahrni, S.M., Fogtmann-Schulz, A., Friedrich, R., Kohler, P., Kudsk, S., Miyake, F., Olsen, J., Reinig, F., Sakamoto, M., Sookdeo, A., Talamo, S., 2020. The IntCal20 Northern Hemisphere radiocarbon age calibration curve (0 55 cal kBP). Radiocarbon 62, 725 757.
- Roberts, R.G., Galbraith, R.F., Olley, J.M., Yoshida, H., Laslett, G.M., 1999. Optical dating of single and multiple grains of quartz from Jinmium rock shelter, northern Australia: part II, results and implications. Archaeometry 41, 365–395.
- Roberts, H.M., Duller, G.A., 2004. Standardised growth curves for optical dating of sediment using multiple-grain aliquots. Radiat. Meas. 38 (2), 241 252.
- Roberts, H.M., Bryant, C.L., Huws, D.G., Lamb, H.F., 2018. Generating long chronologies for lacustrine sediments using luminescence dating: a 250,000 year record from Lake Tana, Ethiopia. Quat. Sci. Rev. 202, 66 77.
- Roberts, H.M., Ramsey, C.B., Chapot, M.S., Deino, A.L., Lane, C.S., Vidal, C., Asrat, A., Cohen, A., Foerster, V., Lamb, H.F., Schabitz, F., Trauth, M.H., Viehberg, F.A., 2021. Using multiple chronometers to establish a long, directly-dated lacustrine record: constraining 600,000 years of environmental change at Chew Bahir, Ethiopia. Ouat. Sci. Rev. 266, 107025.
- Russell, J.M., Johnson, T.C., 2007. Little ice age drought in equatorial Africa: intertropical convergence zone migrations and El Nino-southern oscillation variability. Geology 35 (1), 21 24.
- Scholz, C.A., Cohen, A.S., Johnson, T.C., King, J.W., Moran, K., 2006. The 2005 Lake Malawi scientific drilling project. Sci. Drill. 2, 17 19
- Scholz, C.A., Johnson, T.C., Cohen, A.S., King, J.W., Peck, J.A., Overpeck, J.T., Talbot, M. R., Brown, E.T., Kalindekafe, L., Amoako, P.Y., Lyons, R.P., 2007. East African megadroughts between 135 and 75 thousand years ago and bearing on early-modern human origins. Proc. Natl. Acad. Sci. USA 104 (42), 16416–16421.
- Scholz, C.A., Shillington, D.J., Wright, L.J.M., Accardo, N., Gaherty, J.B., Chindandali, P., 2020. Intrarift fault fabric, segmentation, and basin evolution of the Lake Malawi (Nyasa) rift, east Africa. Geosphere 16 (5), 1293 1311.
- Scholz, C.A., Lyons, R., 2022. Gridded bathymetry and profile locations for LakeLake Malawi (Nyasa), east Africa (within Malawi, Tanzania, Mozambique). IEDA. https://doi.org/10.26022/IEDA/330930.

- Smedley, R.K., Skirrow, G.K.A., 2020. Luminescence dating in fluvial settings: overcoming the challenge of partial bleaching. In: Herget, J., Fontana, A. (Eds.), Palaeohydrology. Geography of the Physical Environment. Springer, Cham.
- Stone, J.R., Westover, K.S., Cohen, A.S., 2011. Late Pleistocene paleohydrography and diatom paleoecology of the central basin of Lake Malawi. Palaeogeogr. Palaeoclimatol. Palaeoecol. 303 (1 4), 51 70.
- Tanaka, M., Girard, G., Davis, R., Peuto, A., Bignell, N., 2001. Recommended table for the density of water between 0 C and 40 C based on recent experimental reports. Metrologia 38 (4), 301.
- Thiesen, M., Scheel, K., Diesselhorst, H., 1900. Untersuchungen über die thermische Ausdehnung von fester und tropfbar flüssigen Korpern. Wissenschaftliche Abhandlungen der Physikalisch-technischen Reichsanstalt 3, 1 70.
- Thomas, N., Nigam, S., 2018. Twentieth-century climate change over Africa: seasonal hydroclimate trends and Sahara Desert expansion. J. Clim. 31, 3349–3370.
- Thomsen, K.J., Murray, A.S., Jain, M., B tter-Jensen, L., 2008. Laboratory fading rates of various luminescence signals from feldspar-rich sediment extracts. Radiat. Meas. 43 (9 10), 1474 1486.
- Tierney, J.E., Russell, J.M., Huang, Y., Damste, J.S., Hopmans, E.C., Cohen, A.S., 2008. Northern hemisphere controls on tropical southeast African climate during the past 60,000 years. Science 322 (5899), 252 255.
- Tierney, J.E., Russell, J.M., Sinninghe Damste, J.S., Huang, Y., Verschuren, D., 2011. Late quaternary behavior of the East African monsoon and the importance of the Congo Air boundary, Quat. Sci. Rev. 30 (7–8), 798–807.
- Tierney, J., Smerdon, J.E., Anchukaitis, K.J., Seager, R., 2013. Multidecadal variability in East African hydroclimate controlled by the Indian ocean. Nature 493 (7432), 389 392
- Trauth, M.H., Deino, A.L., Bergner, A.G., Strecker, M.R., 2003. East African climate change and orbital forcing during the last 175 kyr BP. Earth Planet Sci. Lett. 206 (3 4), 297 313.
- Trauth, M.H., Maslin, M.A., Deino, A., Strecker, M.R., 2005. Late Cenozoic moisture history of east Africa. Science 309 (5743), 2051–2053.
- Trauth, M.H., Maslin, M.A., Deino, A.L., Strecker, M.R., Bergner, A.G., Dühnforth, M., 2007. High-and low-latitude forcing of Plio-Pleistocene East African climate and human evolution. J. Hum. Evol. 53 (5), 475–486.
- United Nations, 2019. World population prospects. Available online: https://population.
- University of Minnesota National Lacustrine Core Repository (LacCore), 1996. Archive of Geosample Data and Information from the University of Minnesota National Lacustrine Core Repository (LacCore). NOAA National Centers for Environmental Information.
- Verschuren, D., 1999. Sedimentation controls on the preservation and time resolution of climate-proxy records from shallow fluctuating lakes. Quat. Sci. Rev. 18 (6), 821–837
- Vollmer, M.K., Bootsma, H.A., Hecky, R.E., Patterson, G., Halfman, J.D., Edmond, J.M., Eccles, D.H., Weiss, R.F., 2005. Deep-water warming trend in Lake Malawi, east Africa. Limnol. Oceanogr. 50 (2), 727 732.
- Wintle, A.G., 1973. Anomalous fading of thermo-luminescence in mineral samples. Nature 245 (5421), 143 144.
- Wintle, A.G., 2008. Luminescence dating of quaternary sediments introduction. Boreas 37 (4), 469–470.
- Wolff, C., Haug, G., Timmermann, A., Sinninghe Damste, J.S., Brauer, A., Sigman, D.M., Cane, M.A., Verschuren, D., 2011. Reduced interannual rainfall variability in East Africa during the last ice age. Science 333 (6043), 743 747.
- World Agroforestry Centre, 2014. Africa rivers [shapefile]. http://landscapeportal.org/layers/geonode:africa_rivers_1#more.
- Zimmerman, S.R.H., Wahl, D.B., 2020. Holocene paleoclimate change in the western US: the importance of chronology in discerning patterns and drivers. Quat. Sci. Rev. 246, 106487.